$ADF300321$

AD

TECHNICAL REPORT ARBRL-TR-02523

(Supersedes IMR Nos. 684, 694 & 706)

COMPUTATIONAL MODELING OF AERODYNAMIC

HEATING FOR XM797 NOSE CAP

CONFIGURATIONS

Walter B. Sturek
Lyle D. Kayser
Donald C. Mylin
Henry Hudgins

September 1983

US ARMY ARMAMENT RESEARCH AND DEVELOPMENT COMMAND
BALLISTIC RESEARCH LABORATORY
ABERDEEN PROVING GROUND, MARYLAND

Approved for public release; distribution unlimited.

DTIC
ELECTE
OCT 0 4 1983

E

83 10 03 048

REPORT DOCUMENTATION PAGE		READ INSTRUCTIONS BEFORE COMPLETING FORM
1. REPORT NUMBER TECHNICAL REPORT ARBRL-TR-02523	2. GOVT ACCESSION NO. AD-A133 684	3. RECIPIENT'S CATALOG NUMBER
4. TITLE (and Subtitle) COMPUTATIONAL MODELING OF AERODYNAMIC HEATING FOR XM797 NOSE CAP CONFIGURATIONS		5. TYPE OF REPORT & PERIOD COVERED Final
		6. PERFORMING ORG. REPORT NUMBER
7. AUTHOR(s) W.B. Sturek, L.D. Kayser, D.C. Mylin & H. Hudgins*		8. CONTRACT OR GRANT NUMBER(s)
9. PERFORMING ORGANIZATION NAME AND ADDRESS U.S. Army Ballistic Research Laboratory ATTN: DRDAR-BLL Aberdeen Proving Ground, Maryland 21005		10. PROGRAM ELEMENT, PROJECT, TASK AREA & WORK UNIT NUMBERS RDT&E 1L162618AH80
11. CONTROLLING OFFICE NAME AND ADDRESS US Army Armament Research & Development Command US Army Ballistic Research Laboratory (DRDAR-BLA-S) Aberdeen Proving Ground, MD 21005		12. REPORT DATE September 1983
		13. NUMBER OF PAGES 45
14. MONITORING AGENCY NAME & ADDRESS(if different from Controlling Office)		15. SECURITY CLASS. (of this report) Unclassified
		15a. DECLASSIFICATION/DOWNGRADING SCHEDULE

16. DISTRIBUTION STATEMENT (of this Report)

Approved for public release, distribution unlimited.

17. DISTRIBUTION STATEMENT (of the abstract entered in Block 20, if different from Report)

18. SUPPLEMENTARY NOTES This report supersedes IMR NOs. 684, 694 & 706.
* Commander
US Army Armament Research and Development Command
ATTN: DRDAR-LCA-F
Dover, NJ 07801

19. KEY WORDS (Continue on reverse side if necessary and identify by block number)

Aerodynamic Heating
Unsteady Heat Conduction
Supersonic Flow

20. ABSTRACT (Continue on reverse side if necessary and identify by block number)

The XM797 is a proposed training round for the 105mm M735 high velocity projectile. This projectile is designed to have a trajectory that closely follows that of the M735 yet have a maximum range of 8km. To achieve this performance the XM797 is designed with a nose cap made of zinc alloy which, due to structural weakening caused by aerodynamic heating and centrifugal loads due to spin, is supposed to fail and result in the projectile breaking apart. This paper summarizes the results of a computational study of the effects of aerodynamic heating for several zinc alloy and steel nose cap

DD FORM 1473 EDITION OF 1 NOV 65 IS OBSOLETE
1 JAN 73

20. ABSTRACT (Continued)

configurations for flight conditions pertinent to the development testing
of the shell. The computational results were obtained using the ABRES Shape
Change Code (ASCC) developed by Acurex/Aerotherm for numerically modeling the
in-depth unsteady temperature response of an ablating reentry vehicle. Examples
of the in-depth temperature response of XM797 nose cap configurations are shown
which demonstrate the capability of the code to predict the effects of ablation,
location of boundary layer transition, projectile preconditioning temperature,
and atmospheric conditions. Comparisons of the computational results to the
results of test firings are shown which have provided assistance in the analysis
of the projectile performance.

TABLE OF CONTENTS

3

LIST OF ILLUSTRATIONS

I. INTRODUCTION

The 105mm XM797 is a proposed training round for the 105mm M735 high velocity projectile. The requirements for this training round pertinent to this study are: (1) closely simulate the trajectory of the M735 for ranges up to 3 km and (2) not exceed a maximum range of 8 km. In order to achieve this performance, the XM797 was designed with a nose cap made of zinc alloy which, due to structural weakening caused by aerodynamic heating and centrifugal loads due to spin, is supposed to fail and result in the projectile breaking apart. The projectile main body is segmented into three parts which are held together by the zinc nose cap. A simplified drawing illustrating the projectile concept and functioning is shown in Figure 1.

Firing tests were conducted at Yuma Proving Ground, Arizona, and Fort Greely, Alaska, in which expected performance goals were not met. In order to obtain a better understanding of the behavior of the zinc alloy nose cap for the test conditions encountered, a computational study was initiated to investigate the in-depth thermal response to aerodynamic heating for proposed nose cap configurations. The computational technique used is the ABRES Shape Change Code (ASCC)[1,2,3] This report summarizes the results of a computational study of the effects of aerodynamic heating for several zinc alloy and steel nose cap configurations pertinent to the flight conditions for the development testing of the XM797 shell.

II. COMPUTATIONAL TECHNIQUE

A. Overview

The ABRES Shape Change Code (ASCC) has been developed over a number of years at a cost of tens of thousands of man-hours and several millions of dollars. The primary purpose of the ASCC is to numerically model the shape

---

1. Dahn, T.J., Cooper, L., Rafinejad, D., Youngblood, S.B., and Kelly, J.T., "Passive Nosetip Technology (PANT II) Program. Volume I. Inviscid Flow and Heat Transfer Modeling for Reentry Vehicle Nosetips," SAMSO-TR-77-11, Space and Missile Systems Organization, Air Force Systems Command, Los Angeles, California 90009, October 1976.

2. Rafinejad, D., Dahn, T.J., Brink, D.F., Abbett, J.J., and Wolf, C.J., "Passive Nosetip Technology (PANT II) Program. Volume II. Computer Users Manual: ABRES Shape Change Code (ASCC)," SAMSO-TR-77-11, Space and Missile System Organization, Air Force Systems Command, Los Angeles, California 90009, October 1976.

3. Sandhu, S.S., and Murray, A.L., "Reentry Vehicle Technology (REV-TECH) Program. Volume III. Improved Capabilities of the ABRES Shape Change Code (ASCC 79)," Acurex Report TR-79-10/AS, Acurex Corporation/Aerotherm, 485 Clyde Avenue, Mountain View, California 94043, prepared for Space and Missile Systems Organization, Air Force Systems Command, Los Angeles, California 90009, July 1979.

history and in-depth unsteady temperature response of an ablating reentry vehicle. The code includes inviscid and boundary layer models to calculate heat transfer distributions and recession rates for a variety of flow conditions.

A simplified flow diagram for the ASCC is shown in Figure 2. BRL has sponsored two studies[4,5] which were performed by Acurex/Aerotherm Corporation to apply the ASCC to predict the aerodynamic heating response of high velocity Army shell and to provide a basis for further studies to be carried out in-house at BRL and LCWSL.

B. Heat Conduction

The heat conduction solution is carried out in two grid systems: (1) a moving body oriented grid (s,r) which is used for the ablating outer layer of the body and (2) a fixed cylindrical coordinate system for the remainder of the body. A simplified computational grid for the unsteady heat conduction computations is shown in Figure 3. The computational technique allows each node to be flagged for identification of material properties. This allows multiple materials to be accounted for in a simple manner. The outer, moving layer is solved for using an implicit finite-difference scheme. The inner region is solved for using an explicit finite-difference scheme. The equation solved in the outer, implicit layer is Equation (1).

$$\rho C_p \frac{\partial T}{\partial t} = \frac{1}{r_b \left(1 + \frac{r}{r_c}\right)} \left\{ \frac{\partial}{\partial s} \left[\left(\frac{r_b}{1 + r/r_c}\right) \kappa \frac{\partial T}{\partial s} \right] \right.$$

$$\left. + \frac{\partial}{\partial r} \left[r_b \left(1 - \frac{r}{r_c}\right) \kappa \frac{\partial T}{\partial r} \right] \right\} + \rho C_p \dot{n} \frac{\partial T}{\partial r}$$

(1)

where

C_p = specific heat

r_o = body circumferential radius of curvature

r_b = $r_o + r \cos\theta$

4. Suchsland, K.E., "Aerothermal Assessment of Projectiles Using the ARRES Shape Change Code (ASCC)," Acurex Report TM-80-31-AS, June 1980.

5. Abbett, M.J., Duiven, R.P., Taub, B., and Beck, R.A.S., "Thermal and Structural Analysis of Training Round Nose Caps," Contract Report ARBRL-CR-00455, U.S. Army Ballistic Research Laboratory/ARRADCOM, Aberdeen Proving Ground, Maryland 21005, May 1981 (AD A100712).

r_c – local streamwise radius of curvature

κ = thermal conductivity

ρ = density

$\dot{n}$ = surface normal recession rate, $\dot{n} = -\dot{r}$

T = temperature

t = time

θ = angle between normal to local surface and axis of symmetry

s = streamwise distance along body

r = distance normal to body surface at s

The equation solved in the inner, explicit region is Equation (2).

$$\rho C_p \frac{\partial T}{\partial t} = \frac{\partial}{\partial x} \left(\kappa \frac{\partial T}{\partial x} \right) + \frac{1}{y} \frac{\partial}{\partial y} \left(y \kappa \frac{\partial T}{\partial y} \right) \qquad (2)$$

In this formulation, the lateral heat flux is assumed to be small compared to the heat flux in the normal direction. The temperatures of computational nodes on the same ray are linked implicitly. The temperatures on adjacent rays are linked explicitly. A very complex iterative procedure is used to solve for the surface temperature and the recession rate normal to the outer surface, $\dot{n}$. This procedure accomplishes the coupling of the in-depth solution with surface reactions, convection, and radiation.

C. Inviscid Flow

The inviscid flow field provides input for computation of the outer bow shock shape and the boundary layer development. The inviscid flow field is modeled in ASCC in three parts: (1) surface pressure distribution, (2) shock shape and shock standoff distance, and (3) flow field details in the shock layer. Surface pressure distributions establish the boundary layer edge velocities while pressure levels are used in the determination of thermodynamic and transport properties. The shock shape affects the heat and mass transfer rates through curved shock effects on the boundary layer edge conditions.

The ASCC surface pressure distributions are calculated using semi-empirical correlations established for supersonic and hypersonic flight of re-entry vehicle nosetip configurations. The correlations are evaluated in each of three regions (A,B,C) of the flow field as indicated in Figure 4. These separate results are then combined to yield the complete pressure distribution.

9

The location of the sonic point is calculated as the first step. After the sonic point is located, the correlations are used to calculate the surface pressure distribution in each of the three regions. This involves application of modified Newtonian relations and curve fits of finite-difference solutions for inviscid flow. The ASCC code also allows the user to input tables of previously determined surface pressure distribution if desired.

The shock shape is predicted based on thin shock layer assumptions using an integral method adapted from the method of Crowell.[6] This method uses decoupled integral forms of the continuity and axial momentum equations along with the specified surface pressure distribution. Using oblique shock relations and the equation of state, conditions behind the shock are evaluated as functions of known free-stream conditions. The local shock angle and the shock standoff distance are the two unknowns. The resulting nonlinear equations are solved using an interative technique. The relatively small nose radii and low Mach (Mach < 5) numbers of interest to the Army are outside the range of applicability of thin shock layer theory and the ASCC method can yield shock angles and shock coordinate values which are inconsistent. These inconsistencies were great enough to cause the code to fail to reach a solution for some geometries.

A modification was made which allows the shock shape to be predicted by quadrature of the shock angle alone. This procedure gives consistent shock angles and shock coordinates for the shapes considered in this study.

Another difficulty encountered with the ASCC shock layer modeling was the technique for determining where the outward normal from the body surface intersected the bow shock. For slender shapes such as the XM797, the original coding could result in "kinked" shock waves that were multivalued both axially and radially. An improved calculational procedure was developed which overcomes this difficulty and has been incorporated by Acurex/Aerotherm in updated versions of ASCC.

D. Viscous Boundary Layer Modeling

The viscous boundary layer determines the wall heat and mass transfer and the wall shear. The predictive method employed is sufficiently sophisticated to include all the important physical events present in the flow field (as long as there are no embedded shock waves in the flow field) and is computationally fast. The basic concept was formulated by Dahn et al[1] and developed into the momentum-energy integral technique (MEIT). The method retains the essential features of the boundary layer equations and accounts for physical events such as blowing, acceleration, roughness, property variation, and inviscid vortical layer effects. The boundary layer methodology is the most important individual feature of ASCC. The basic governing equations and the methodology are outlined below.

6. Crowell, P.G., "Shock Shape Calculation in Body Oriented Coordinates for Specified Surface Pressure," Aerospace Corporation Memo 76-5134.5-019, May 1976.

The boundary layer momentum and energy integral equations are

$$(1/r) \frac{d}{ds} (r\rho_e u_e^2 \theta) = \tau_w + (\rho v)_w u_{i,w} + H\theta \frac{dp}{ds} \qquad (3)$$

and

$$(1/r) \frac{d}{ds} (r\rho_e u_e (h_{t,e} - h_w)\phi) = q_w + (\rho v)_w (h_{t,i,w} - h_w). \qquad (4)$$

The various quantities that appear in the above integral equations are defined as:

momentum thickness θ:

$$\theta = \int_0^\infty \left(\frac{\rho u}{\rho_e u_e}\right) \frac{u_i - u}{u_e} \, dy \qquad (5)$$

energy thickness ϕ:

$$\phi = \int_0^\infty \left(\frac{\rho u}{\rho_e u_e}\right) \frac{h_{t,i} - h_t}{h_{t,e} - h_w} \, dy \qquad (6)$$

boundary layer shape factor:

$$H = \delta^*/\theta \qquad (7)$$

displacement thickness δ^*:

$$\delta^* = \int_0^\infty \left(1 - \frac{\rho u}{\rho_i u_i}\right) dy \qquad (8)$$

The subscript e refers to properties evaluated at the boundary layer edge; the script i refers to inviscid properties evaluated along the stagnation point isentrops. The quantity $u_{i,w}$ is the inviscid velocity at the wall. (The terms $h_{t,i}$ and $h_{t,e}$ refer to local and edge inviscid stagnation enthalpies, respectively, which are the same for atmospheric flight.) For nonvortical inviscid outer flow, $u_i = u_e$, $h_{t,i} = h_{t,e}$ and $\rho_i = \rho_e$; and the above equations reduce to standard integral boundary layer equations.

11

To solve the equations, the properties at the edge of the boundary layer are needed. This input is obtained by using the inviscid flow solutions and an entrainment relation which accounts for the entropy change due to shock curvature. Dahn et al,[1] based on theory and experimental data, developed correlations of skin friction, Stanton number, and auxiliary relations for solving the governing equations. The auxiliary relations consist of a series of influence coefficients which account for complex interaction effects between physical processes. The influences modeled include Reynolds number, Mach number, boundary layer conditions (laminar, transitional, or turbulent), surface roughness, mass transfer, and flow field acceleration. The solution procedure consists of two steps: (1) Series solutions at and in the vicinity of the stagnation point are obtained. (2) A finite-difference scheme is used to obtain solutions away from the stagnation region. Initial information required includes: (1) surface shape, (2) surface pressure, (3) blowing rate, and (4) temperature distribution.

III. COMPUTATIONAL RESULTS

A. Overview

The results presented here represent a small portion of the total computational effort expended in this study of the aerodynamic heating for the XM797 projectile. The intent here is to summarize the results in a manner that will preserve the overall scope of the results, indicate the modeling capability inherent in the ASCC code, and discuss uncertainties discovered in comparison of the computational and experimental results.

It may be surmised that the input data to ASCC is quite complex and requires substantial background and experience to select correct values for the many input parameters. In order to short circuit the time required to gain this experience, a STAS (Short Term Analysis Services) contract was carried out with Acurex[5] to exercise the code for several Army shell applications. This served as the starting point for the computational studies carried out at BRL and LCWSL for the XM797 projectile.

The results will cover basically three configurations of the XM797 nose cap: (1) all zinc, (2) plug nose (steel tip with zinc afterbody), and (3) all steel.

B. All-Zinc Nose --- Thermal Simulation Tests

The all-zinc nose represents an interesting challenge for the ASCC since the ability to model ablation with the accompanying shape change is required. An example of the grid system used for the XM797 is shown in Figure 5. The locking pin protrusion into the nose cap is modeled by flagging appropriate grid nodes for the material properties of mild steel. The location of "critical node B" is indicated. This node was selected because it was judged to be in the area of expected failure for the nose cap. (Critical nodes "A" and "C" are discussed later.) Although the actual failure position is not known, this node served as a basis for comparison between computational results and experimental test data. A series of computations was carried out to examine the influence of the computational grid resolution on the predicted

12

in-depth temperature response and ablation of the nose cap. The results indicated a decided sensitivity for surface temperature; however, the in-depth temperature at the critical node was not strongly affected. The results to be shown here used the maximum array capacity built into the code. The implicit grid was 10 x 29 and the explicit grid was 60 x 25.

Melting produces a layer of liquid at the surface whose flow along the body is not considered in the ablation modeling of ASCC. Although modeling of the actual mass distribution of the melt was not attempted, it was possible to extend empirically the existing representation of transition, turbulent surface roughness, and laminar heating augmentation. This was done by specifying: (1) a melting temperature for each material, (2) temperatures at which melting induces transition, (3) the temperature at which laminar heating is augmented by a specified amount due to melting, and (4) the temperature at which turbulent roughness heating is augmented. All of these phenomena are assumed to be caused by melting but their corresponding temperatures need not be the melt temperature. These degrees of freedom allow additional adjustment of the model to improve agreement with experimental data on melting surfaces.

After analyzing two data sources on zinc noses of different designs (NASA Ames thermal wind tunnel tests[7] and actual firing tests[8]), it was determined that the recession rate of an all-zinc nose was closely matched by an effective turbulent roughness of molten zinc of about 20 mils, a laminar heating augmentation factor of 10, and fixing transition at the most forward point on the zinc surface that had melted. In practice, it was found necessary for numerical stability to apply a ramp in roughness and heating augmentation rather than a step at the specified temperature for the physical phenomenon. This ramp extends over roughly 5° F on both sides of the specified temperature.

Some experiments have been conducted in the AVCO arc jet on all-zinc noses.[9] Figure 6 shows the stagnation point recession as a function of time for the runs available (12357 and 12370). Repeatability of the test results was not good. The variation may be due to the random size and location of voids in the cast zinc noses. There are X-ray data and sectioned noses that confirm the existence and prevalence of such voids.

Computational predictions using the previously determined 20 mils turbulent roughness follows the early trend of Run 12357 well, particularly the time of onset of nose recession, but falls below the experimental data after one second. An equivalent roughness at melt of 50 mils was also tried (see

7. Schwind, Richard G., "Hypersonic Wind Tunnel Tests of Nose Cap Models Utilizing Shape Change for Range Control," Nielsen Engineering and Research, Inc., NEAR TR 184, March 1979.

8. Fleming, G.C., "Maximum Range Test Results of the 105mm, XM797 Training Projectile Conducted Between January and October 1980 at Yuma Proving Ground, Arizona," ASD IR-2-82, December 1981.

9. Loeb, A., LCWSL unpublished experimental data. Private communication.

Figure 6) and comes closer but is still below the experimental results. Run 12370 has the same time of onset of recession as Run 12357 but has a consistently higher recession rate and is, of course, even further above the predicted recession.

Since more detail can be computed in the nose region when the origin of the rays of the polar grid system is closer to the nose, the origin was moved to OX = 0.6; see Figure 5 (using 50 mils roughness). The computed result, shown in Figure 6, shows recession beginning too early but matching the results at later times for Run 12357 very well. Numerical difficulties are known to exist with the current grid system for the nose region of a slender body, and an improved system is currently being developed on contract. The porosity of the zinc nose is another unknown and unmodeled effect that contributes to the discrepancies described above.

Melting and ablation are similar in that the energy balance involves latent heats. However, there is a large difference in the magnitude of the latent heats for melting and ablation. Both ablation and melting are in-depth phenomena, but they are modeled in the current version of the ASCC code as surface phenomena. This difficulty is also being addressed in the current contractural effort.

C. All-Zinc Nose --- Atmospheric Flight Conditions

Different thermal/structural analyses had resulted in different conjectures for the failure points and modes in the nose (see Figure 7), the leading candidates being shearing or opening of the threads in the zinc at point A, bending failure at point B, or hoop stress failure at point C. Therefore, an attempt was made to see if a unique temperature at one "critical point" could correlate the flight tests results for a range of wall thicknesses, launch velocities, initial temperatures, and ambient temperatures.

The velocity-time trajectory for the XM797 launched at standard atmospheric conditions is plotted in Figure 8. An example of the predicted shape of the nose cap at several times in the flight is shown in Figure 9. The temperature of the surface at one second of flight is given in Figure 10. The extent of the melt layer is clearly indicated by the region of constant temperature of 1179 R.

Examination of typical computed temperature histories at the points of interest (see Figure 11) shows that the histories are quite nonlinear as a function of time. An exponential rise is a simple form that approximates the trend of the actual behavior.

$$\frac{T_m - T}{T_m - T_1} = ae^{bt} \tag{9}$$

The form of Equation (9) was used to correlate predicted temperatures with observed breakup (failure) times for points A, B, and C for selected test data. Each group resulted in a different temperature of breakup at the same location, with maximum spreads of 20° to 80° F. The correlation coefficients

14

produced by Equation (9) for the 3 locations examined were: $\rho_1(A) = -0.970$, $\rho_1(B) = -0.467$, $\rho_1(C) = -0.963$.

The longest experimental time to breakup correlated poorly at points A, B, and C. One hypothesis to explain this result is that molten zinc flows onto the cooler steel body and re-solidifies. This possibility is not considered in the computational modeling. The results from the plasma arc jet tests show that this phenomenon does occur--model disassembly after testing revealed zinc solidified inside the split aft body segments.

The important correlation is predicted breakup time versus experimental breakup time. The mean temperature at breakup was used to obtain the time of predicted breakup. These results are plotted in Figures 12 to 14. The correlation coefficients for these cases are: $\rho_t(A) = 0.717$, $\rho_t(B) = 0.550$, $\rho_t(C)$ = 0.867. Point C at the rear interface between the nose and the body clearly correlates best. The mean temperature at breakup time there is 544K. The arc jet tests at AVCO clearly showed failure at point C in the hoop stress mode.

D. Plug Nose Modeling

The plug nose geometry was devised in an effort to overcome two of the difficulties identified in testing of the all-zinc configuration: (1) higher drag due to nosetip ablation and (2) inconsistent performance. A simplified drawing of the plug nose configuration is given in Figure 15. The shape consists of a steel tip and an afterbody with a zinc ring. The proposed failure mode still relies on the melting or thermal weakening of the zinc due to aerodynamic heating.

Computations were made for various surface rou_inesses, differing boundary layer transition criteria, and trajectories with different initial projectile temperatures. Examination of BRL experimental data (aerodynamic range spark shadowgraphs) indicated that the ASCC was predicting boundary layer transition too early based on surface length and free-stream conditions. The experimental data indicate that the transition Reynolds number (Re_s) should be about

4.3×10^6 whereas the code predicts $Re_s \approx 1.3 \times 10^6$. The code also allows for prediction of transition using a momentum thickness criterion. Figure 16 shows an example of the sensitivity of the in-depth temperature response of the critical node (B) to the location of boundary layer transition. Using the criteria built into the code, the critical node is predicted to reach melt temperature within roughly two seconds of flight. Forcing transition to occur further downstream results in the critical node never reaching the melt temperature. These computations indicate that boundary layer transition can have a significant effect on the in-depth temperature response of the XM797 configuration. The variation in predicted heat transfer coefficient at time one second for several transition criteria is shown in Figure 17. The location of boundary layer transition is easily identified by the increase in heat transfer coefficient.

A series of experimental firings for different projectile preconditioning temperatures (cold: 244K, standard: 294K, and hot: 322K) was performed at Yuma Proving Ground, Arizona. Using a boundary layer transition criterion of

15

$Re_s = 1.75 \times 10^6$, a series of computational results was obtained for flow conditions matching the firing tests. A comparison between the computational results for the critical node temperature history and the experimentally observed projectile breakup times is given in Figure 18. The notation "B/U" indicates time of projectile breakup as determined from Doppler radar data. This figure shows that the experimental observations correlate qualitatively with the computational predictions. A failure criterion is implied for a critical node temperature of about 556K.

E. Solid Steel Nose Modeling

A series of computations was run for nose caps made of solid steel in an effort to identify in-depth regions of high temperature gradients. Examples of these computational results are shown as temperature contours in Figures 19a through 19f for specific times in the trajectory. The results indicate that very high temperature gradients occur only near the leading edge of the projectile and that the temperature gradients become noticeably less severe throughout the projectile tip after one second of flight.

In an effort to evaluate the effect of the location of boundary layer transition on the performance of the XM797, a series of computations was carried out for different locations of boundary layer transition (X_{TR}). The results are shown in Figure 20 where the time for the critical node to reach 556K is plotted versus X_{TR} for two projectile preconditioning temperatures. These results indicate an inherent sensitivity of the design concept to atmospheric conditions even if the location of boundary layer transition could be fixed using a boundary layer trip.

IV. SUMMARY

This paper has described a computational study in which the ABRES Shape Change Code (ASCC) has been applied to predict the in-depth temperature response to aerodynamic heating of XM797 nose cap configurations. Results have been shown which provide examples of the ability of the code to predict effects of ablation, location of boundary layer transition, projectile preconditioning temperature, and atmospheric conditions. Comparison of the computational results to the results of test firings provided assistance in the analysis of the projectile performance, including identification of the failure point and failure mode for the all-zinc noses.

The experience gained in the course of this study has resulted in the identification of several desirable modifications to the code which would enhance its application to problems of interest in shell design. A contract with Acurex/Aerotherm is nearing completion which will result in the code having: (1) an improved grid configuration for long, slender shell; (2) an interactive graphics computational grid generation routine; (3) improved modeling of in-depth melt and contact resistance between materials; and (4) capability for planar 2D predictions for swept fins.

16

A lesson learned in this study is that aerodynamic heating cannot reliably cause a functioning late in the flight where the aerodynamic heating input is reduced. Any desired event to be caused by aerodynamic heating must occur early in the flight where the heat transfer rate is high.
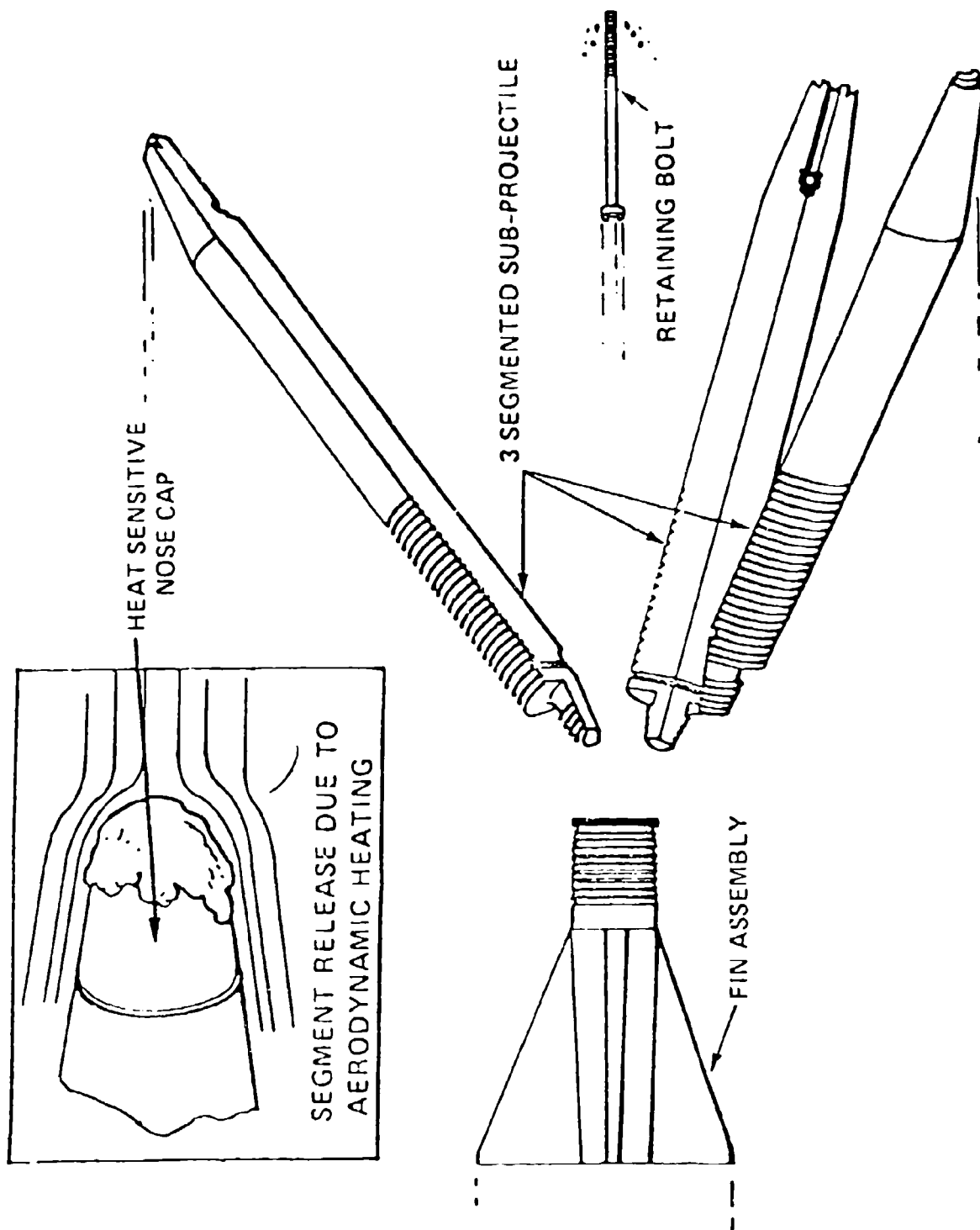
HEAT SENSITIVE NOSE CAP

3 SEGMENTED SUB-PROJECTILE

RETAINING BOLT

SEGMENT RELEASE DUE TO AERODYNAMIC HEATING

FIN ASSEMBLY

Figure 1. Schematic Illustration of the 105mm XM797 Projectile Concept

SIMPLIFIED FLOW CHART FOR ASCC

```
                    ┌──────────────┐   PROJECTILE SHAPE
                    │  INPUT DATA  │   MATERIAL PROPERTIES
                    └──────────────┘   FREE STREAM CONDITIONS
                           │           VELOCITY-TIME HISTORY
                    ┌──────────────────┐
                    │ SURFACE PRESSURE │
                    │   SHOCK SHAPE    │
                    └──────────────────┘
                           │
          ┌────────────────────────────────┐
          │  BOUNDARY LAYER DEVELOPMENT     │
          └────────────────────────────────┘
                           │
                    ┌──────────────┐
                    │ SURFACE ENERGY│
                    │     AND      │
                    │ MASS BALANCE │
                    └──────────────┘
                           │
                    ┌──────────────┐
                    │ SHAPE CHANGE │
                    └──────────────┘

INCREMENT TIME

                    ┌──────────────┐
                    │   IN-DEPTH   │
                    │  CONDUCTION  │
                    └──────────────┘
```

PRIMARY LOOP ⇉
INTERACTIVE LOOP →
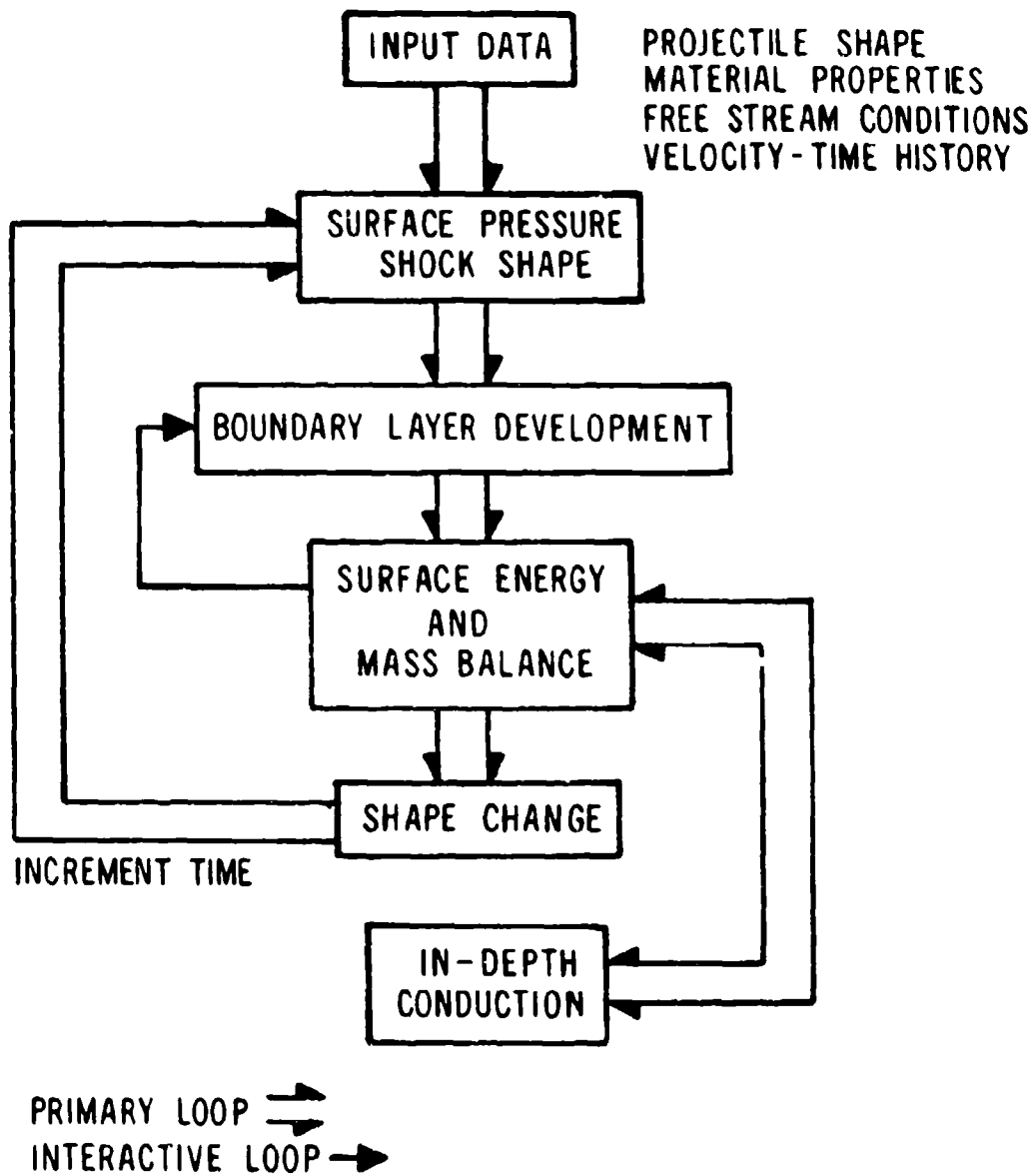
Figure 2. Simplified Flow Chart for ASCC

19
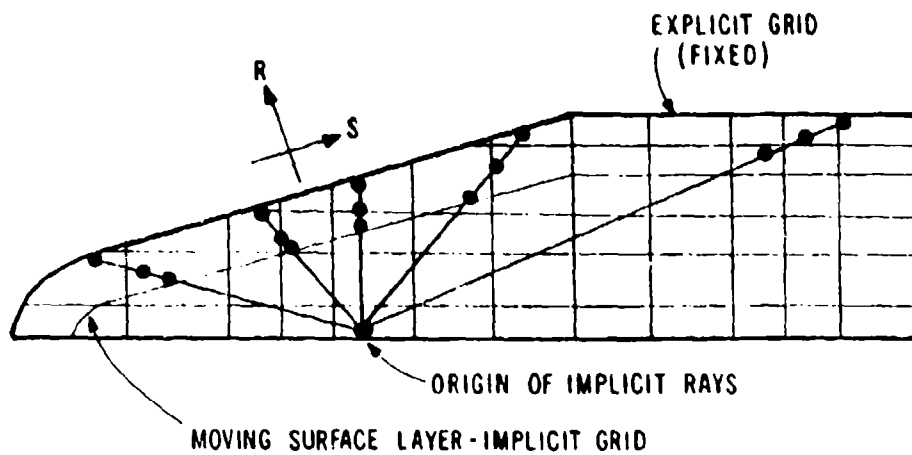
Figure 3. Simplified Computational Grid for Heat Conduction Solution
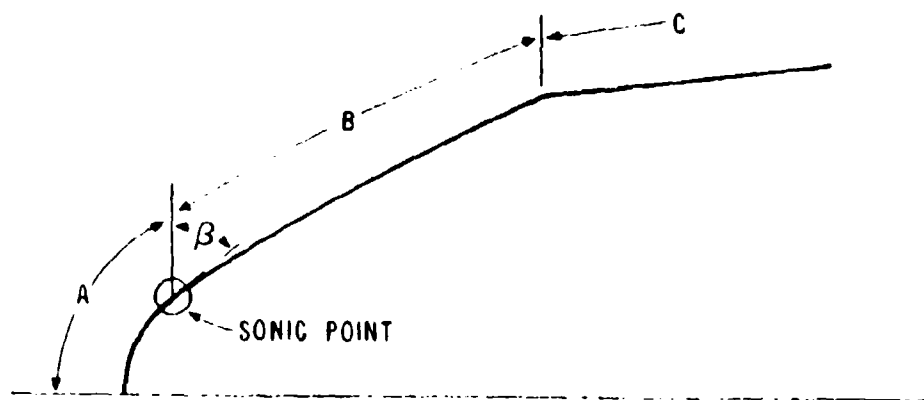
Figure 4. Three Regions for Inviscid Flow Modeling

20
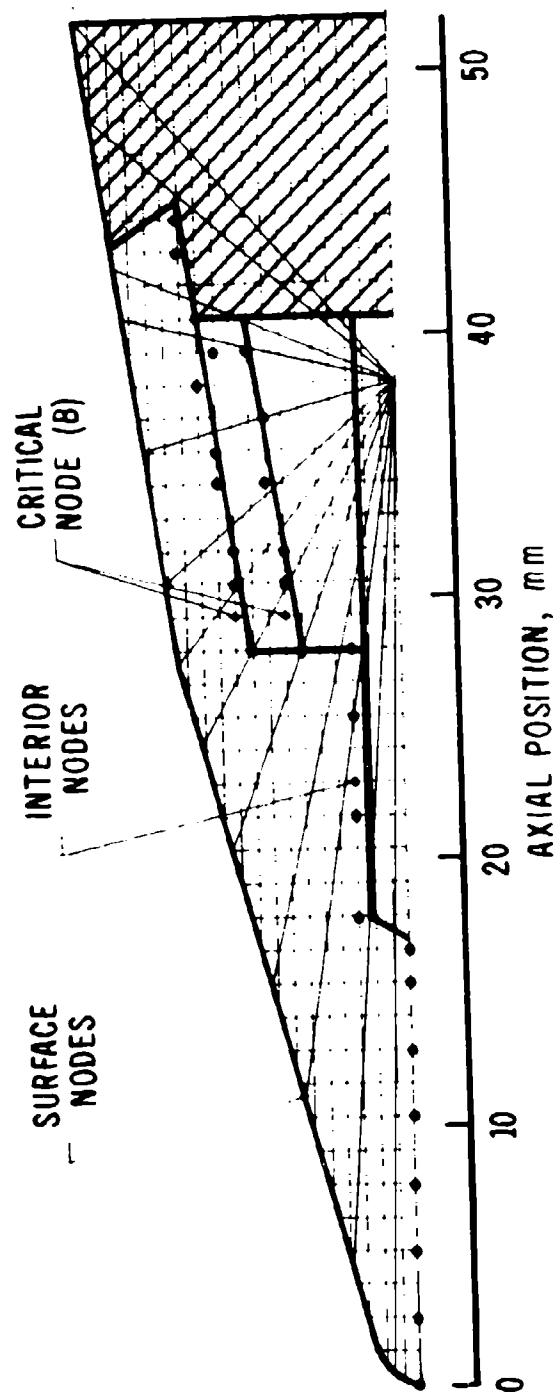
Figure 5. Computational Grid for the XM797
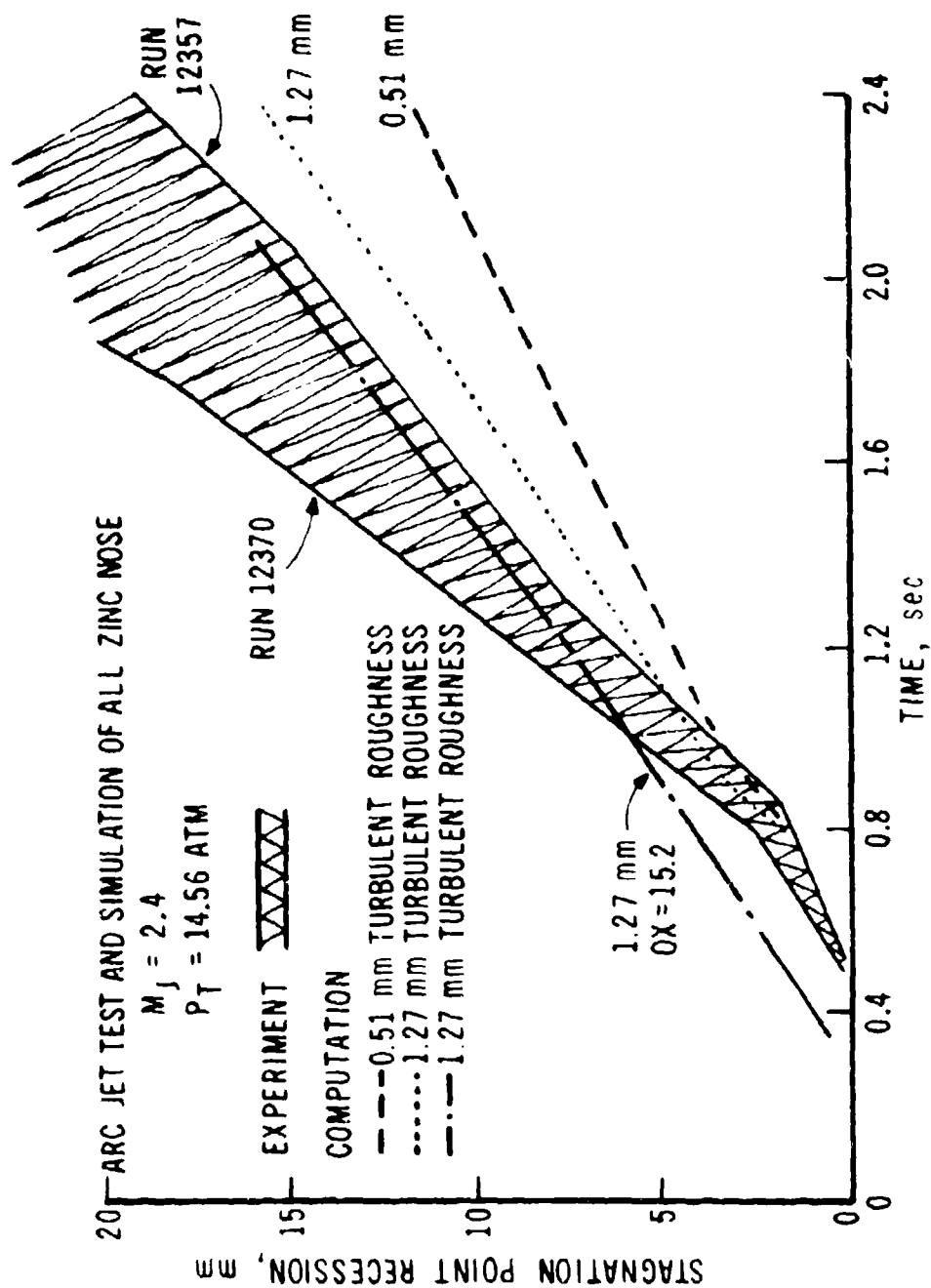
Figure 5. Stagnation Point Recession-Arc Jet Test Data
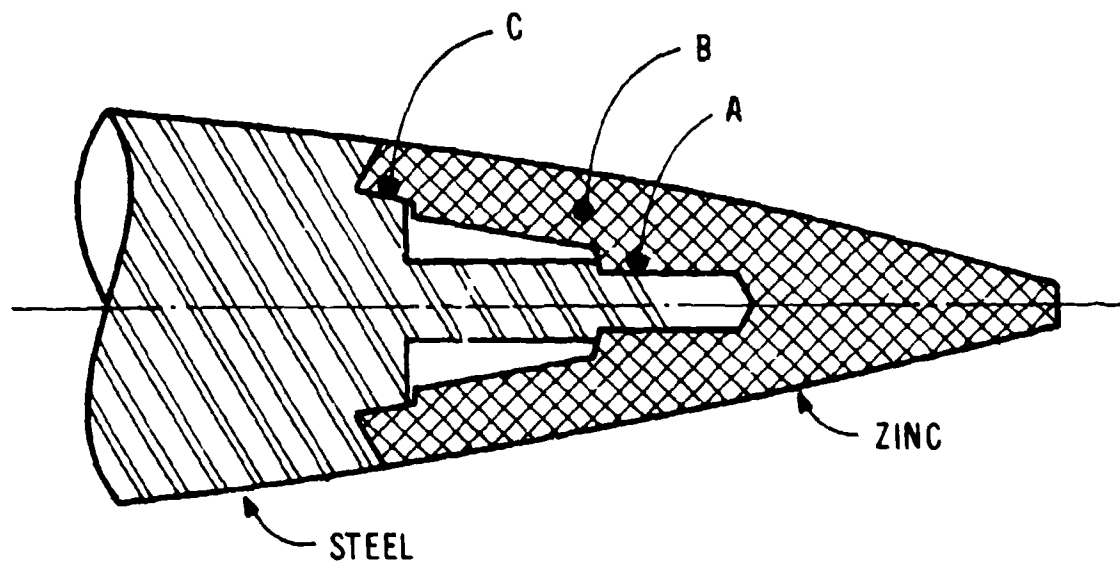
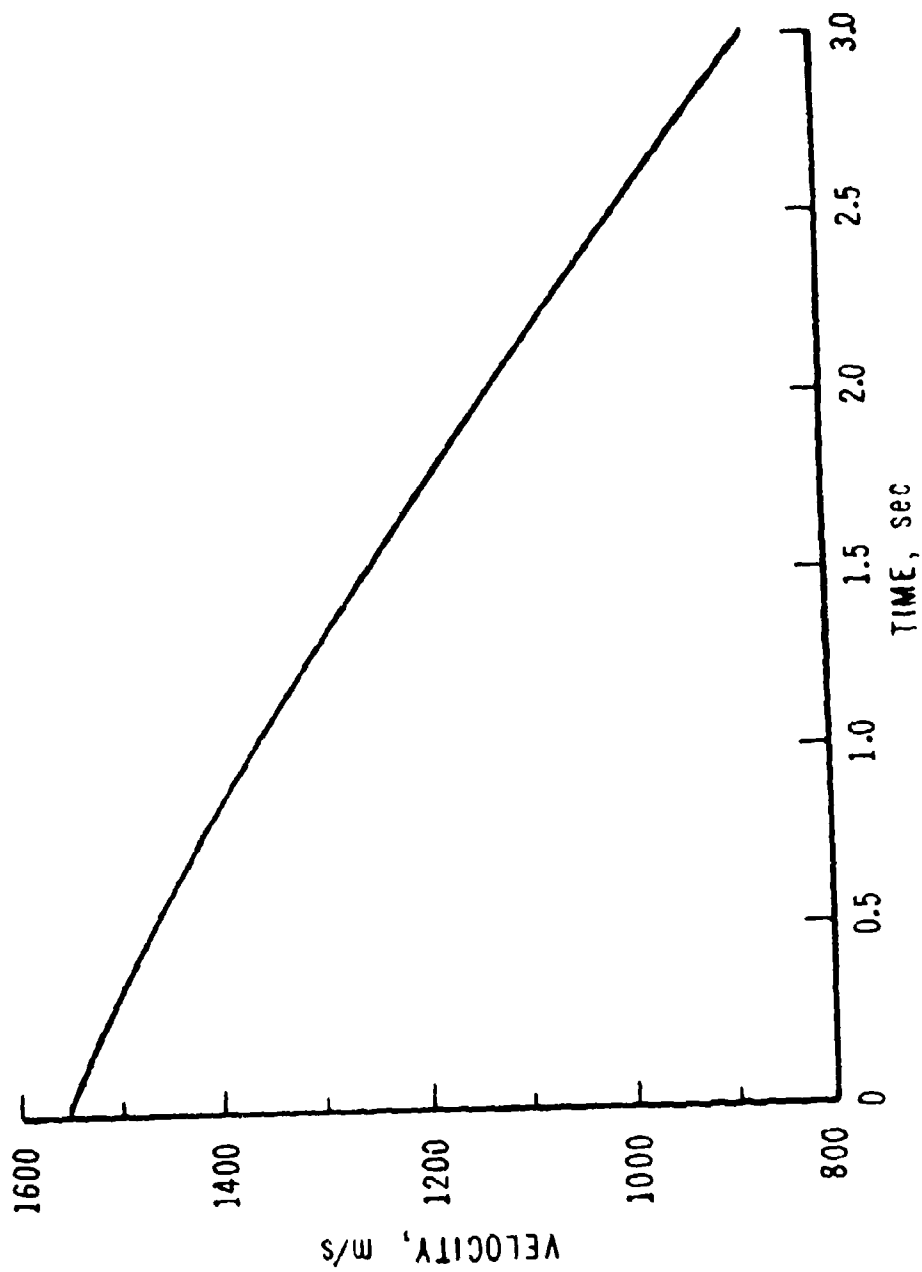Figure 7. Simplified Drawing of XM797 Nose Cap Showing Critical Points

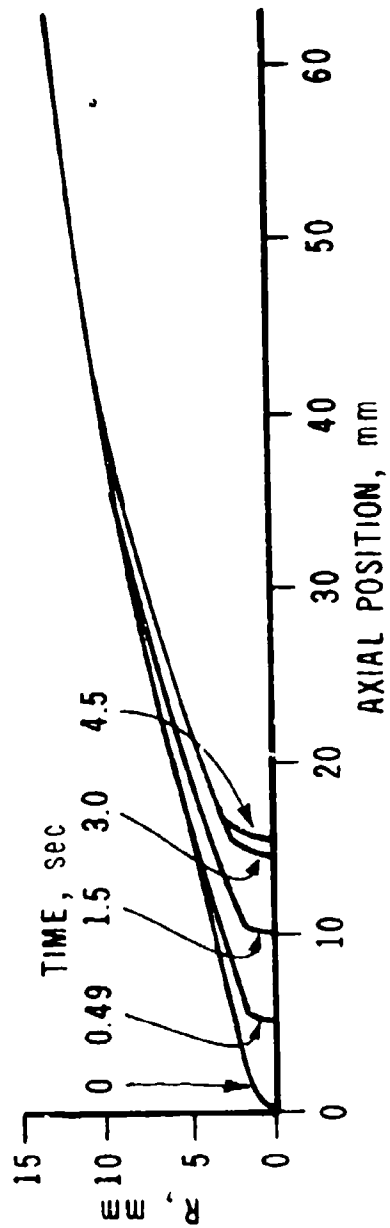Figure 3. Velocity-Time History for the XM797 Launched at Standard Atmospheric Conditions

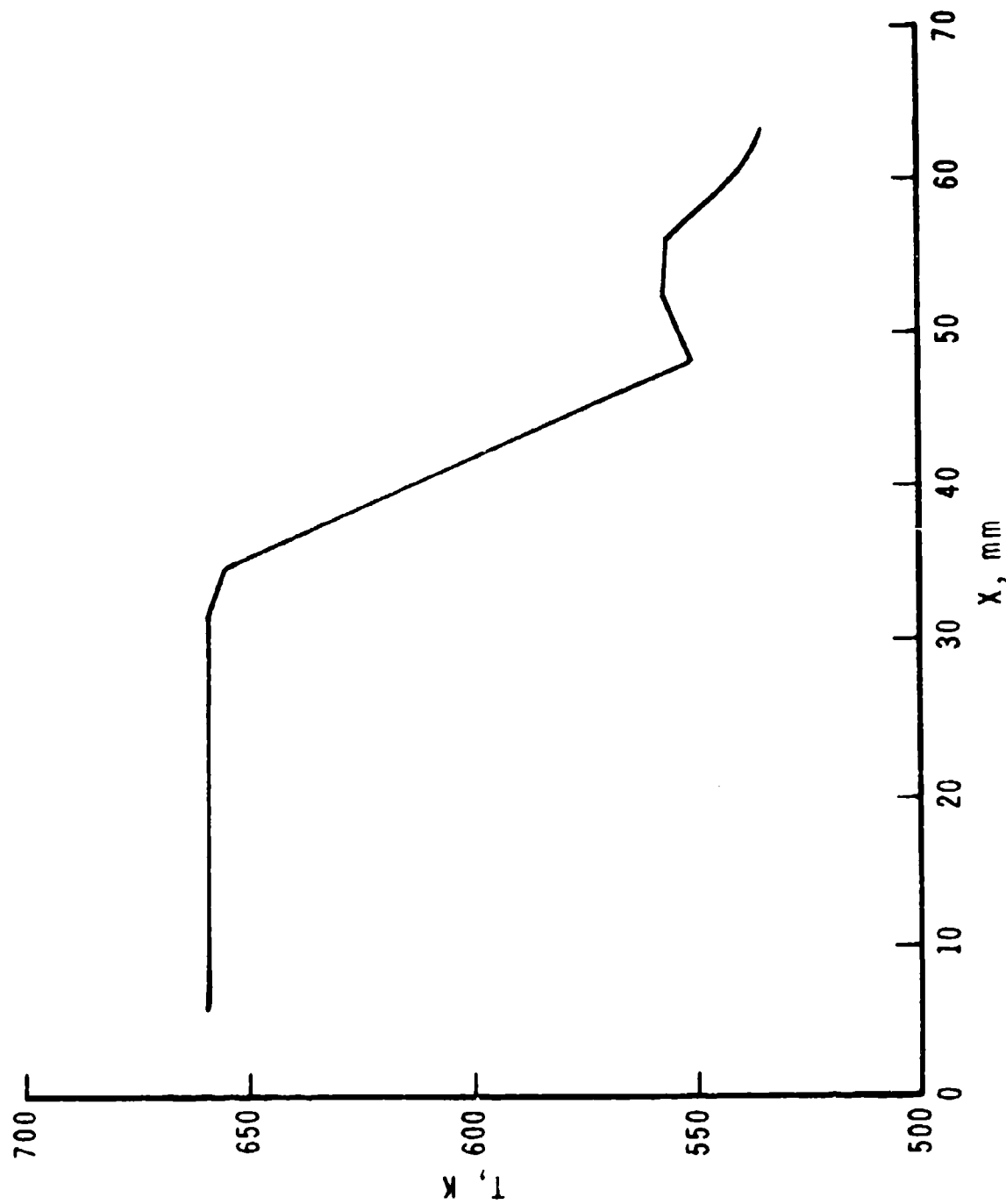Figure 9. Zinc Nose Cap Recession-Atmospheric Flight Prediction

Figure 10. Surface Temperature at Time = One Second - Atmospheric Flight Prediction

26
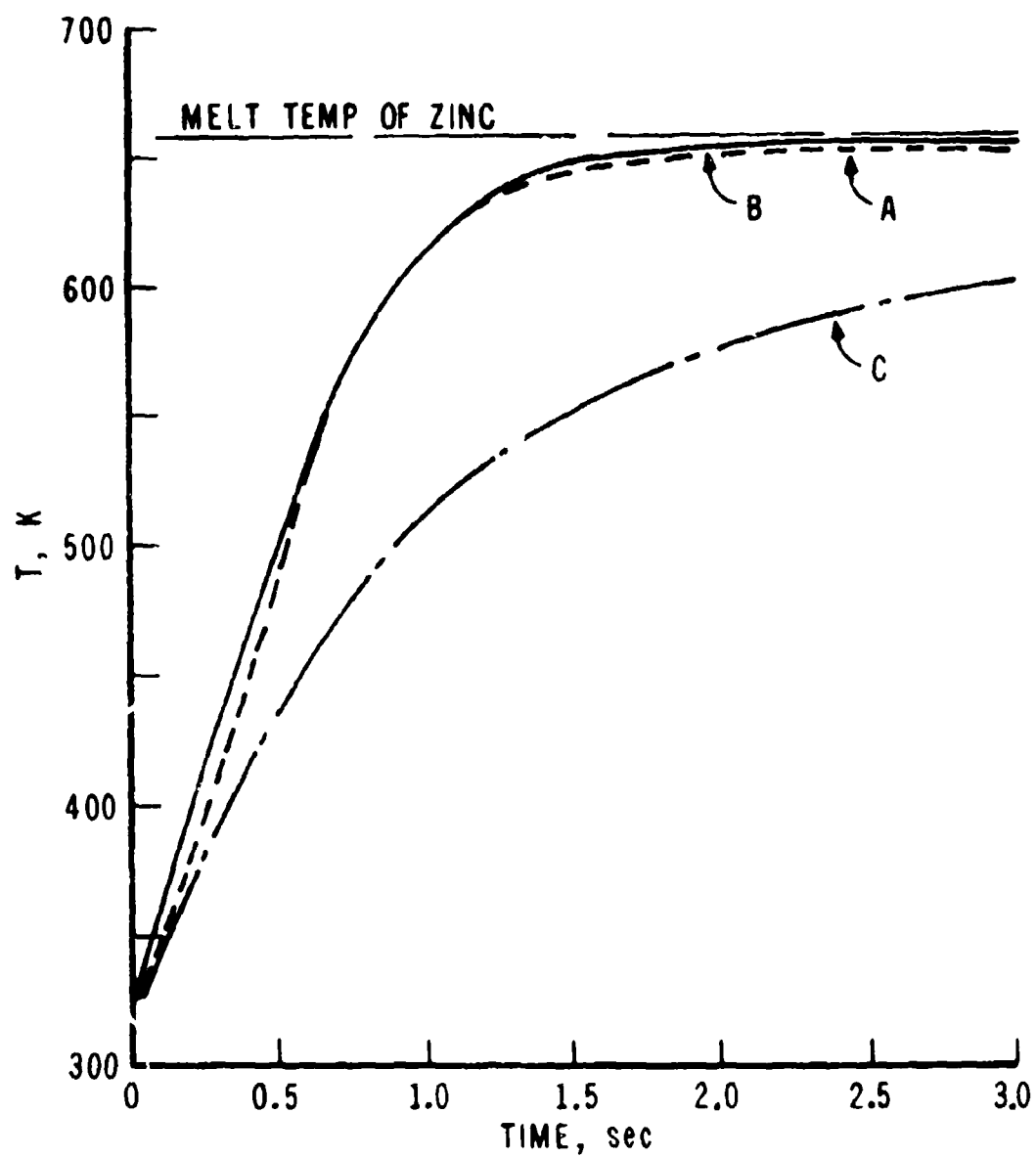
Figure 11. In-Depth Temperature History at Critical Nodes A, B, and C
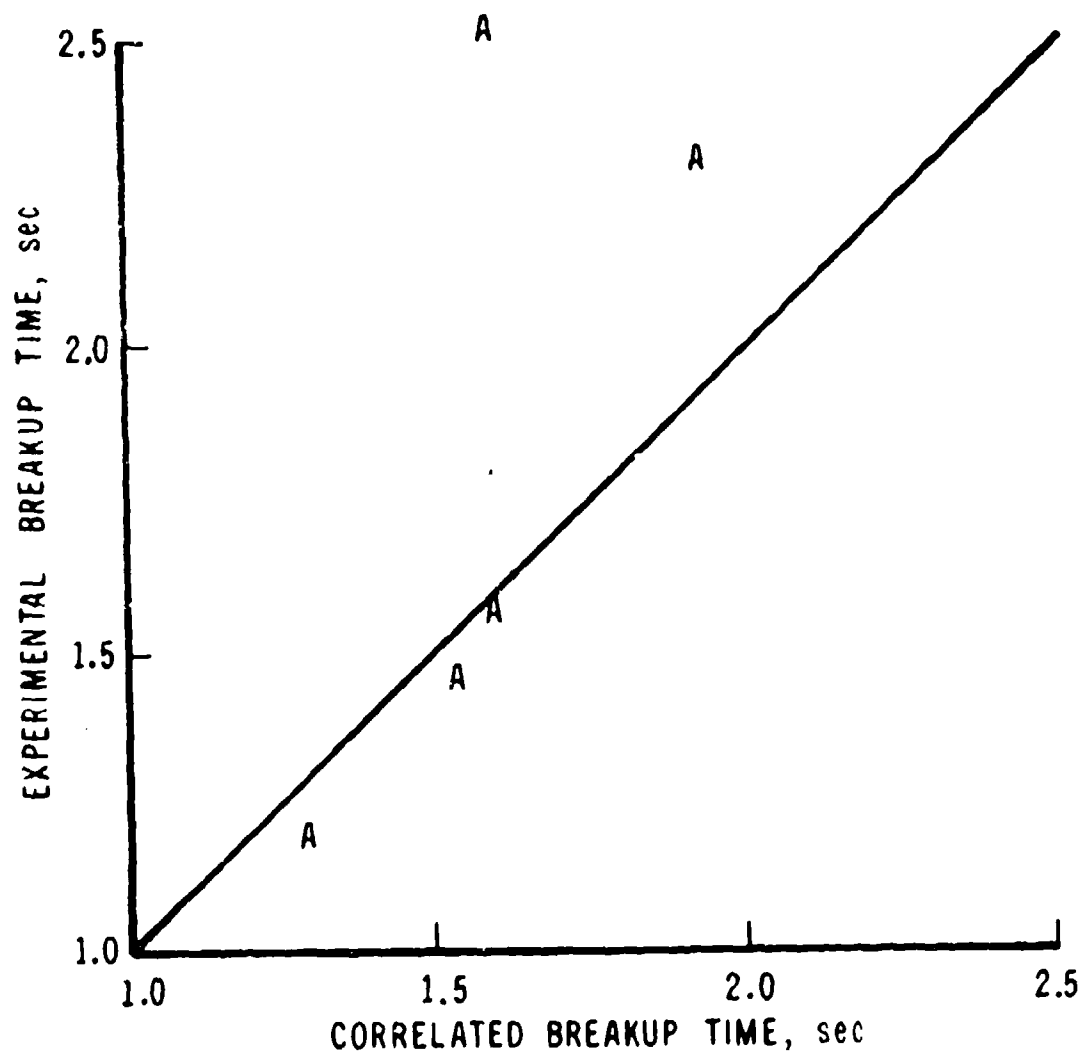
Figure 12. Correlation of Breakup Times, Critical Node A
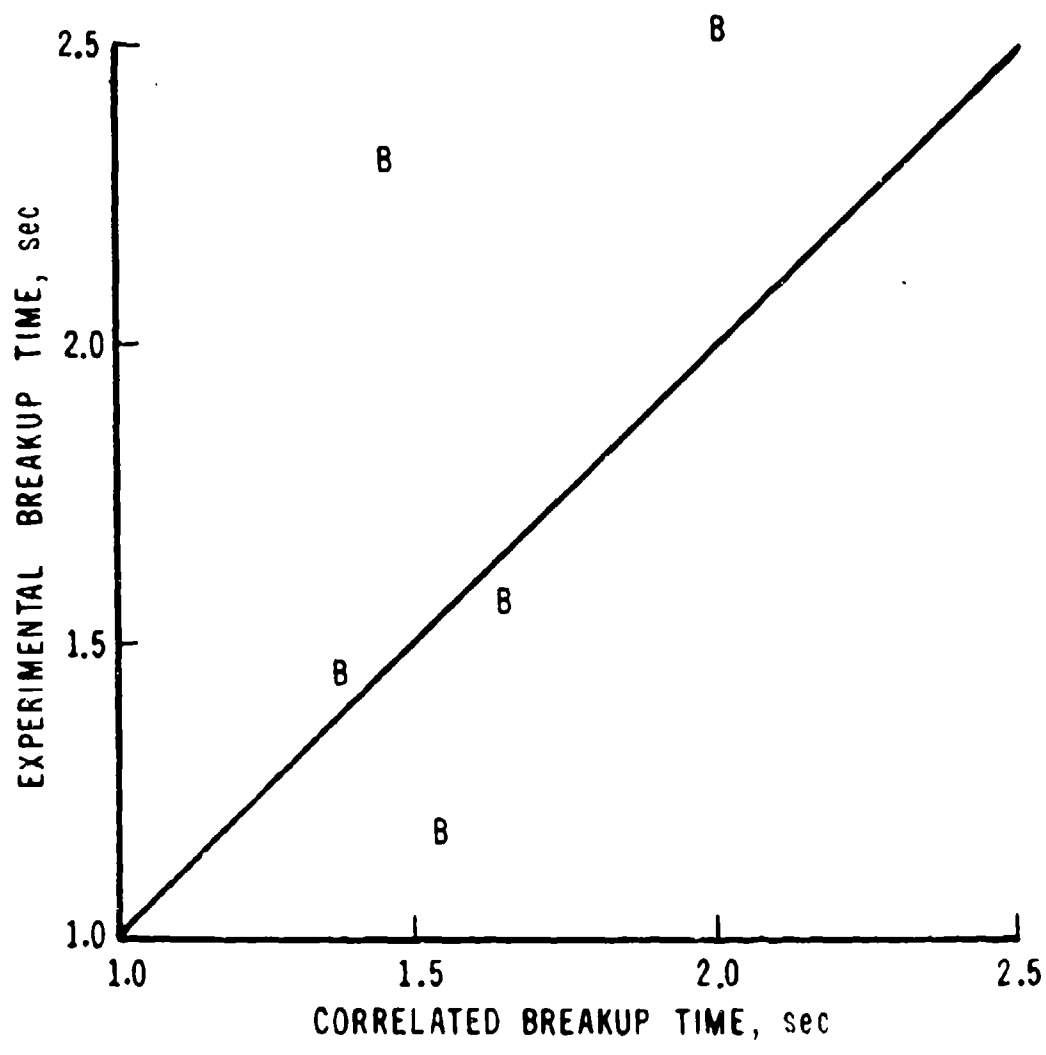
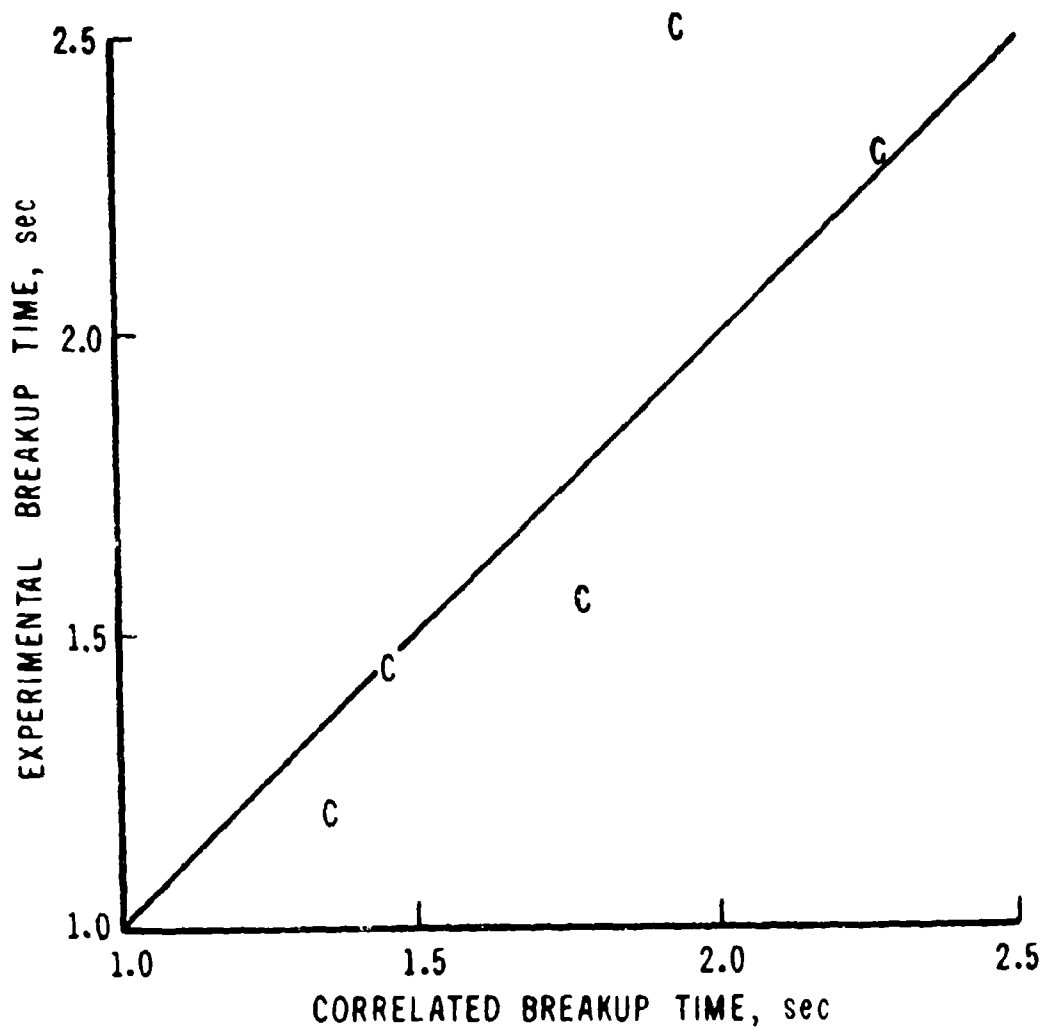Figure 13. Correlation of Breakup Times, Critical Node B

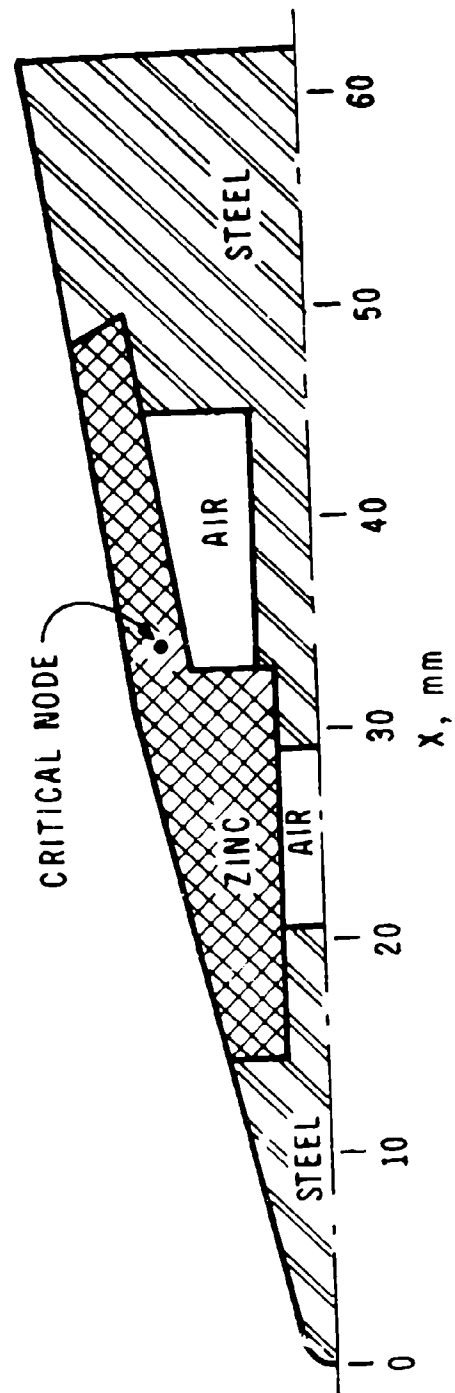Figure 14.   Correlation of Breakup Times, Critical Node C

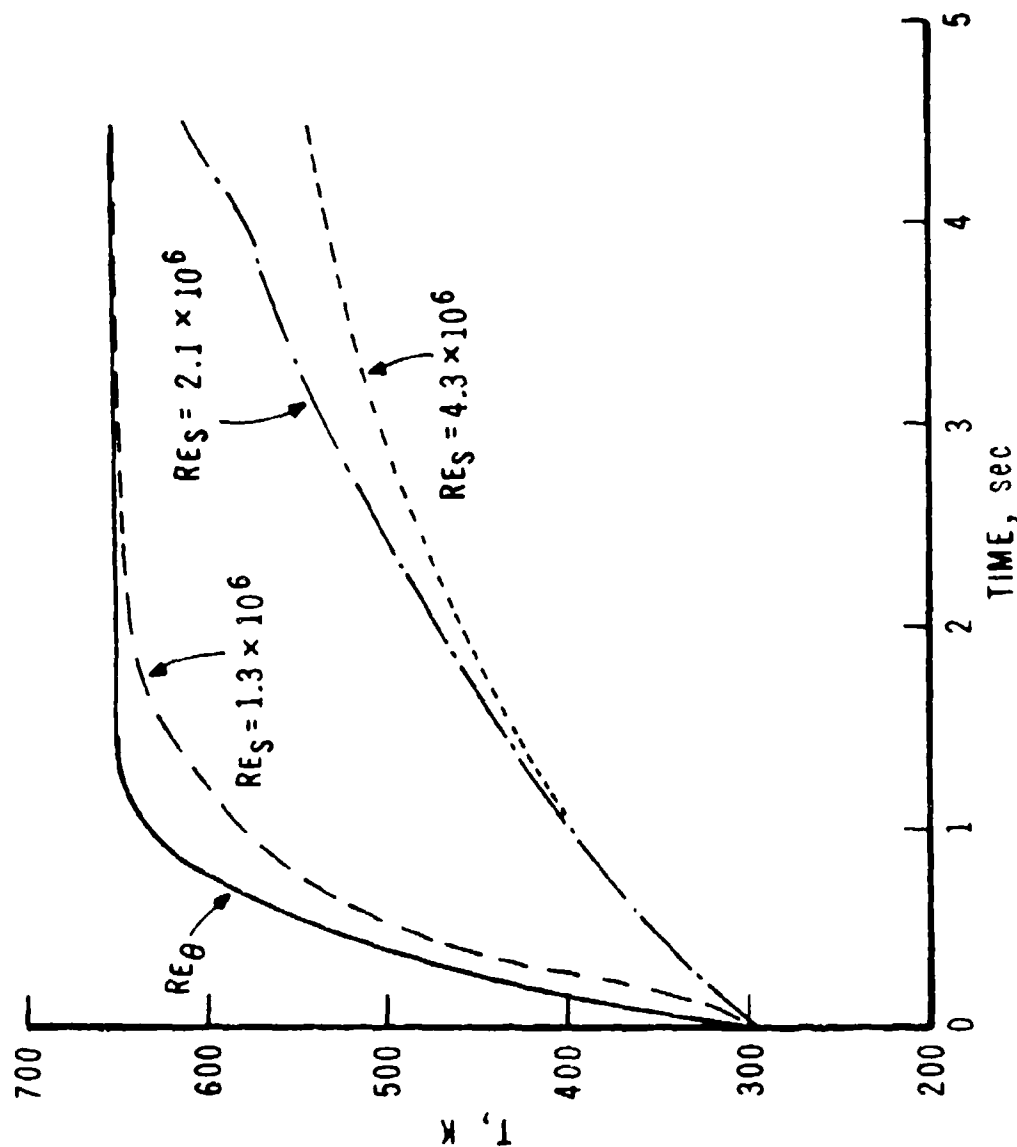Figure 15. Simplified Drawing of the Plug Nose Configuration

Figure 16. In-Depth Temperature Response of Critical Node B Comparing Different Criteria for Boundary Layer Transition
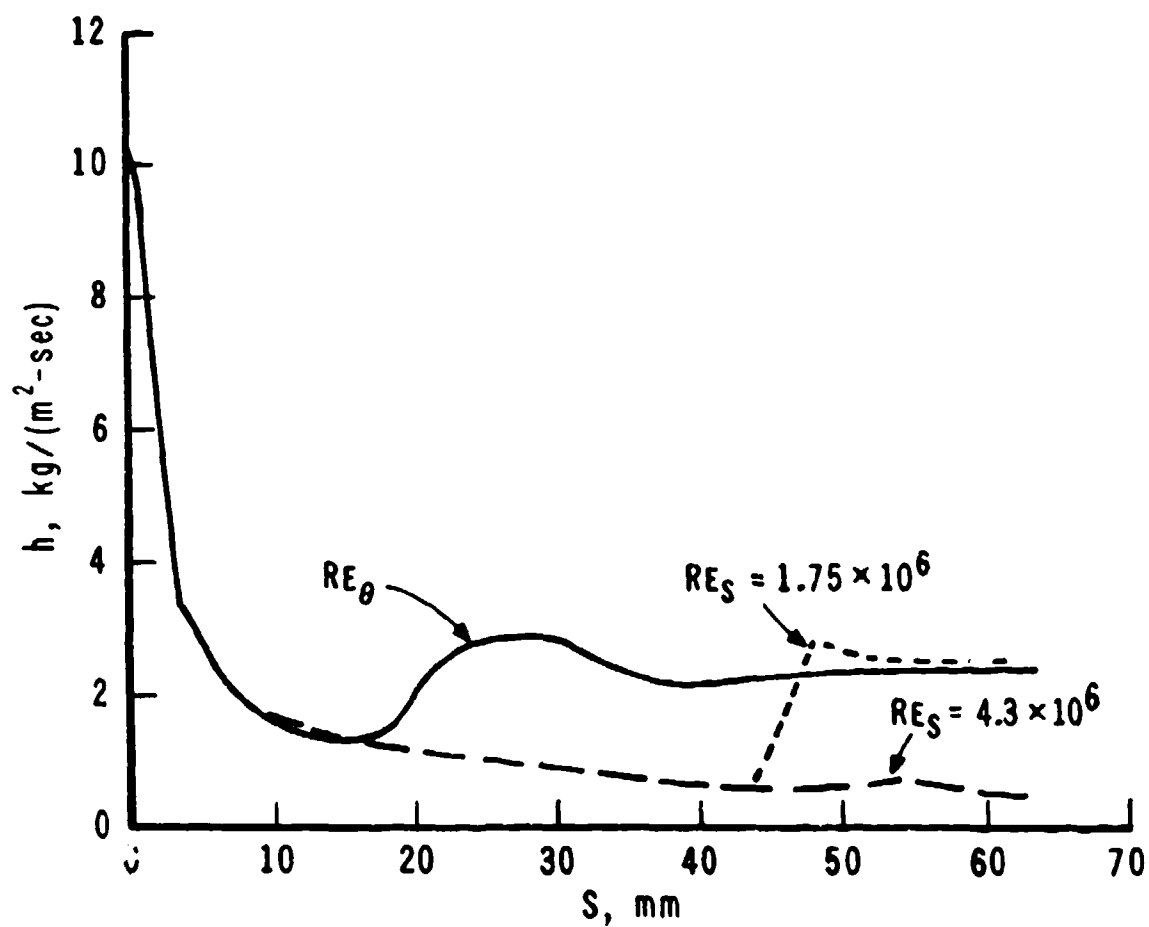
32

Figure 17. Distribution of Heat Transfer Coefficient for Several
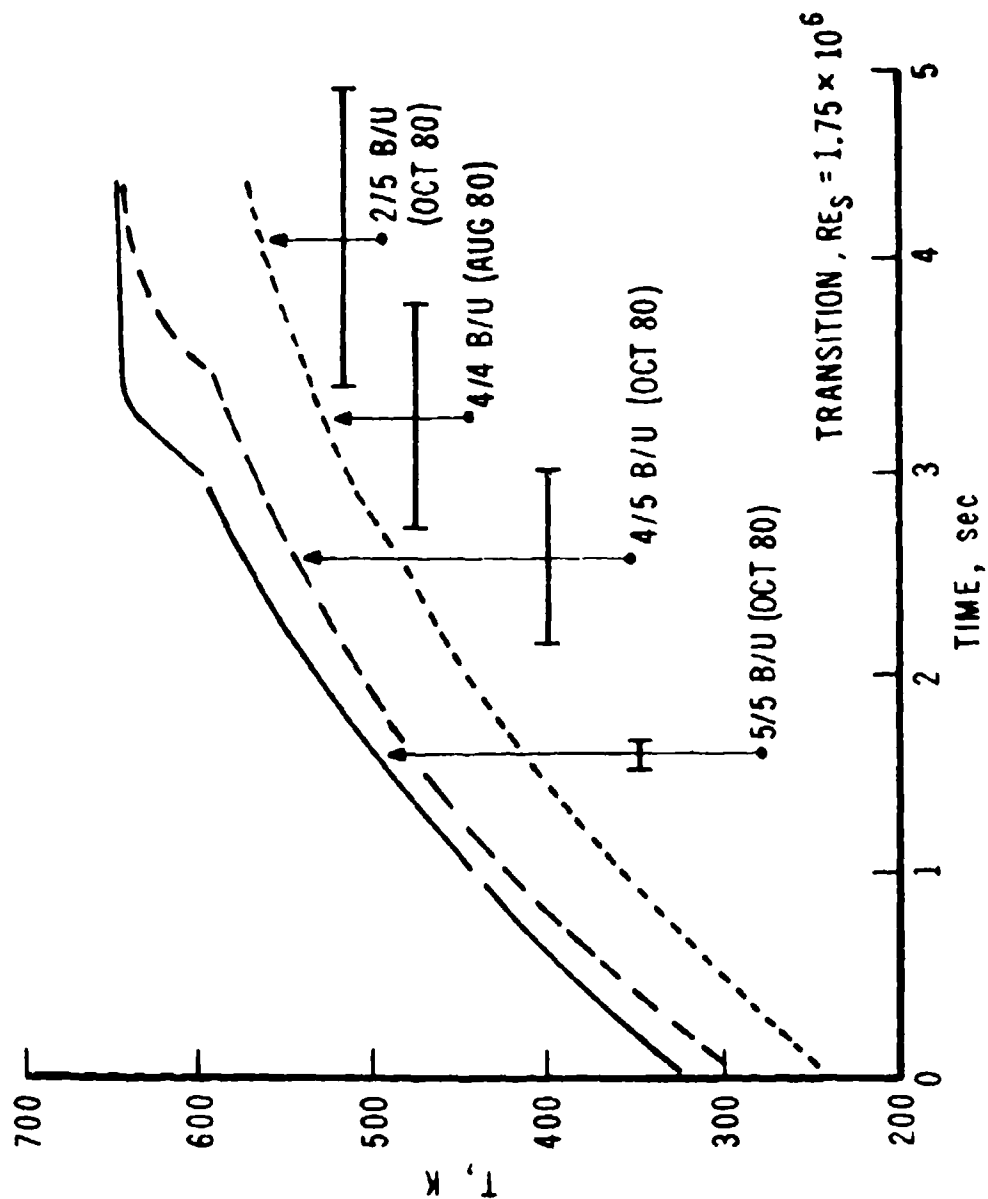Criteria for Boundary Layer Transition

Figure 18. Comparison of In-Depth Temperature Response to Projectile Breakup Observed Experimentally
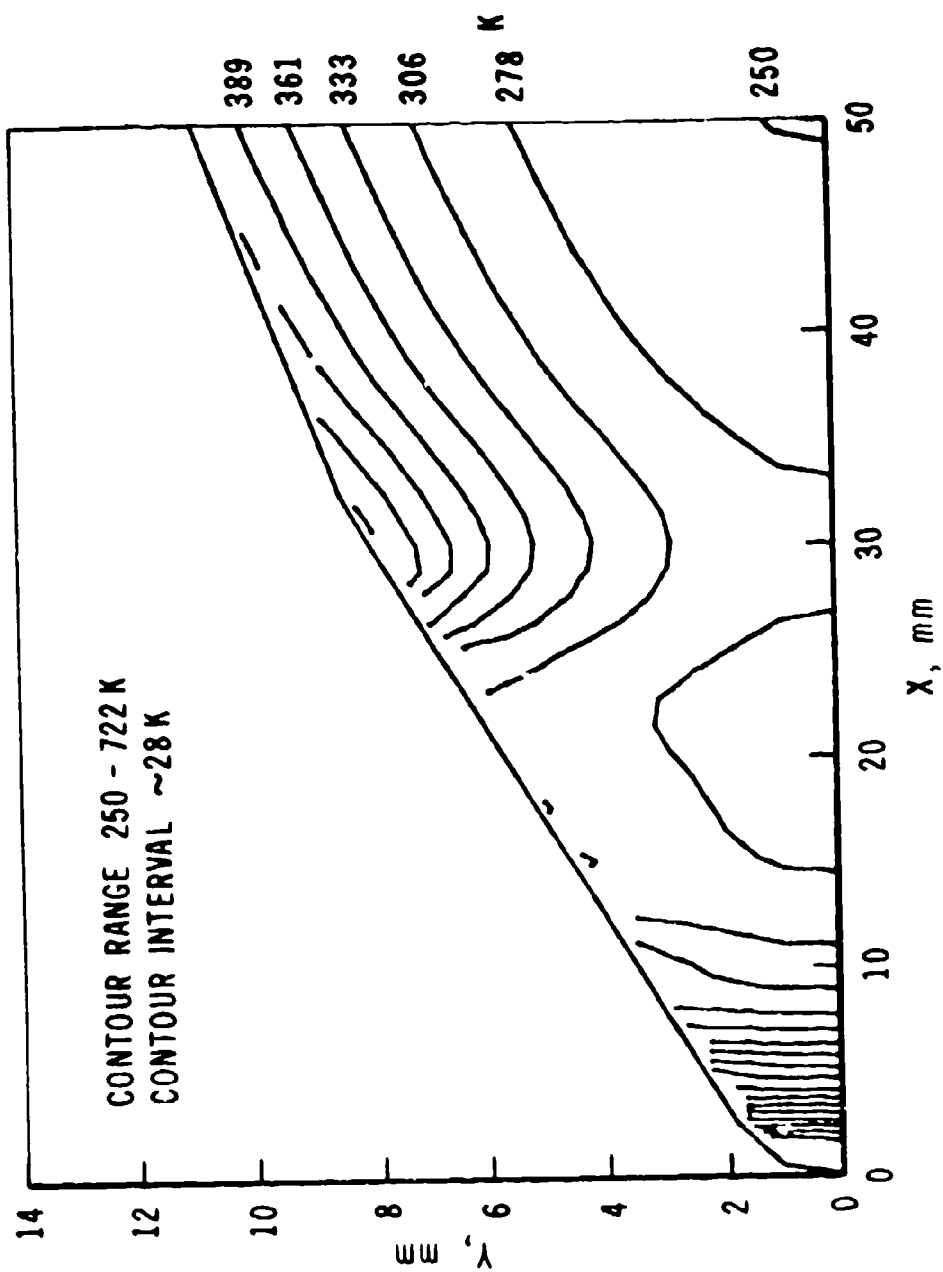
Figure 19. In-Depth Temperature Contours for All-Steel Nose

a. Time = 0.5 Second
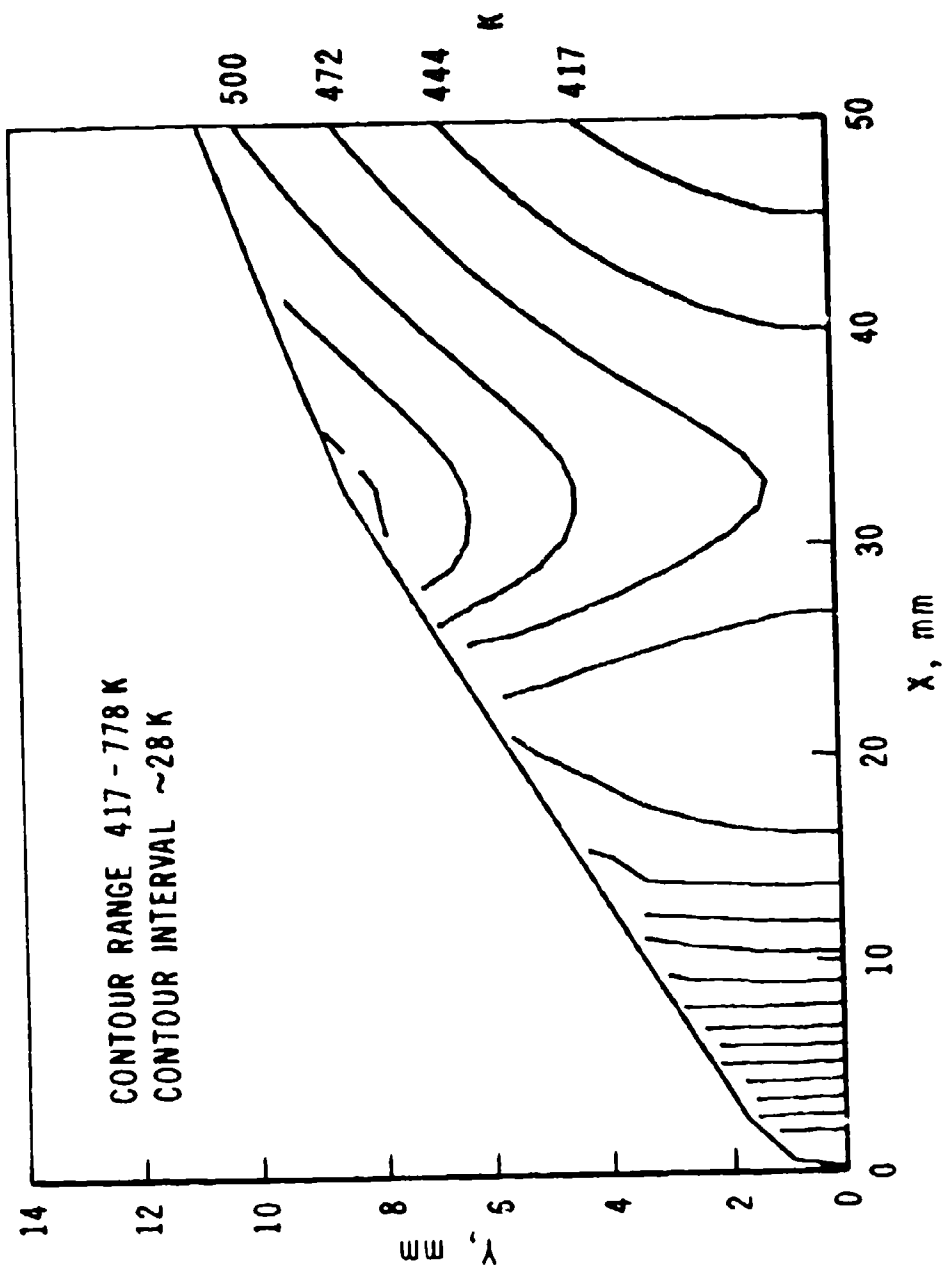
Figure 19. Continued

b. Time = 1.0 Second

CONTOUR RANGE 417 – 778 K
CONTOUR INTERVAL ~28 K

CONTOUR RANGE 361 - 806 K
CONTOUR INTERVAL ~28 K

472
444
417
389 K
361

X, mm

Y, mm
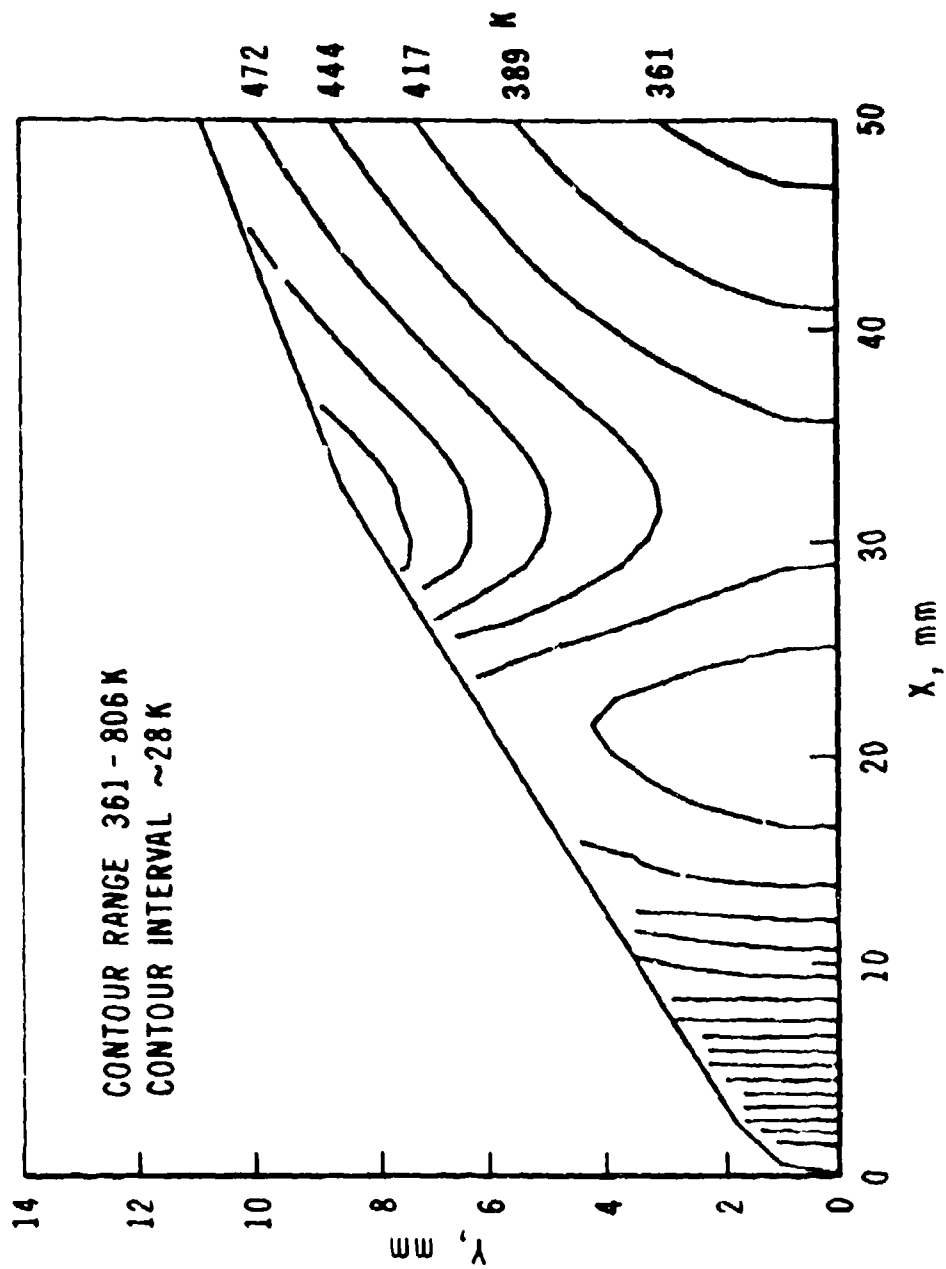
Figure 19. Continued

c. Time = 1.5 Seconds

CONTOUR RANGE 417-778 K
CONTOUR INTERVAL ~28 K
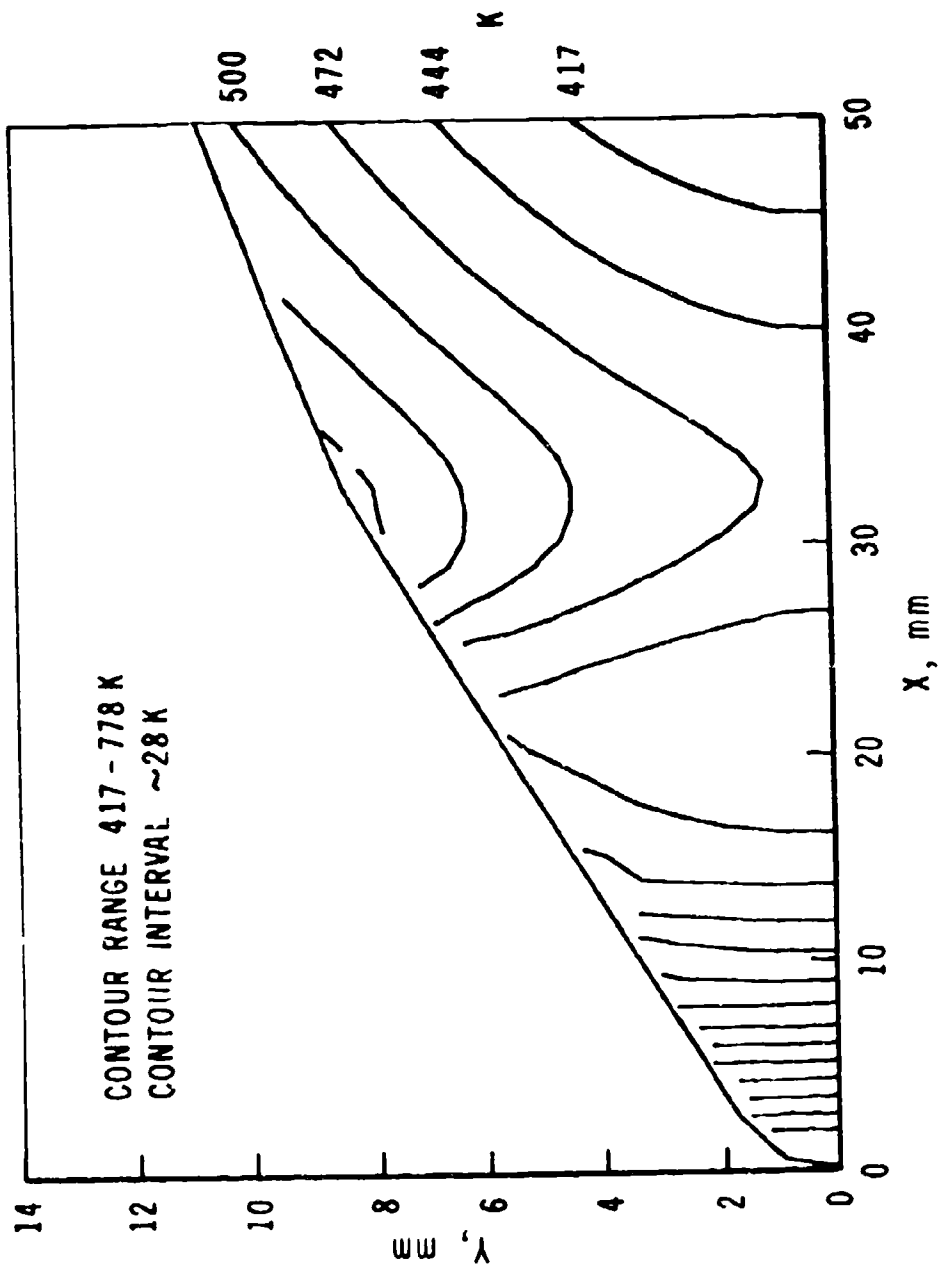
Figure 19. Continued

d. Time = 2.0 Seconds

38

CONTOUR RANGE 444-750 K
CONTOUR INTERVAL ~28 K

Figure 19. Continued

e. Time = 2.5 Seconds

CONTOUR RANGE 472-750 K
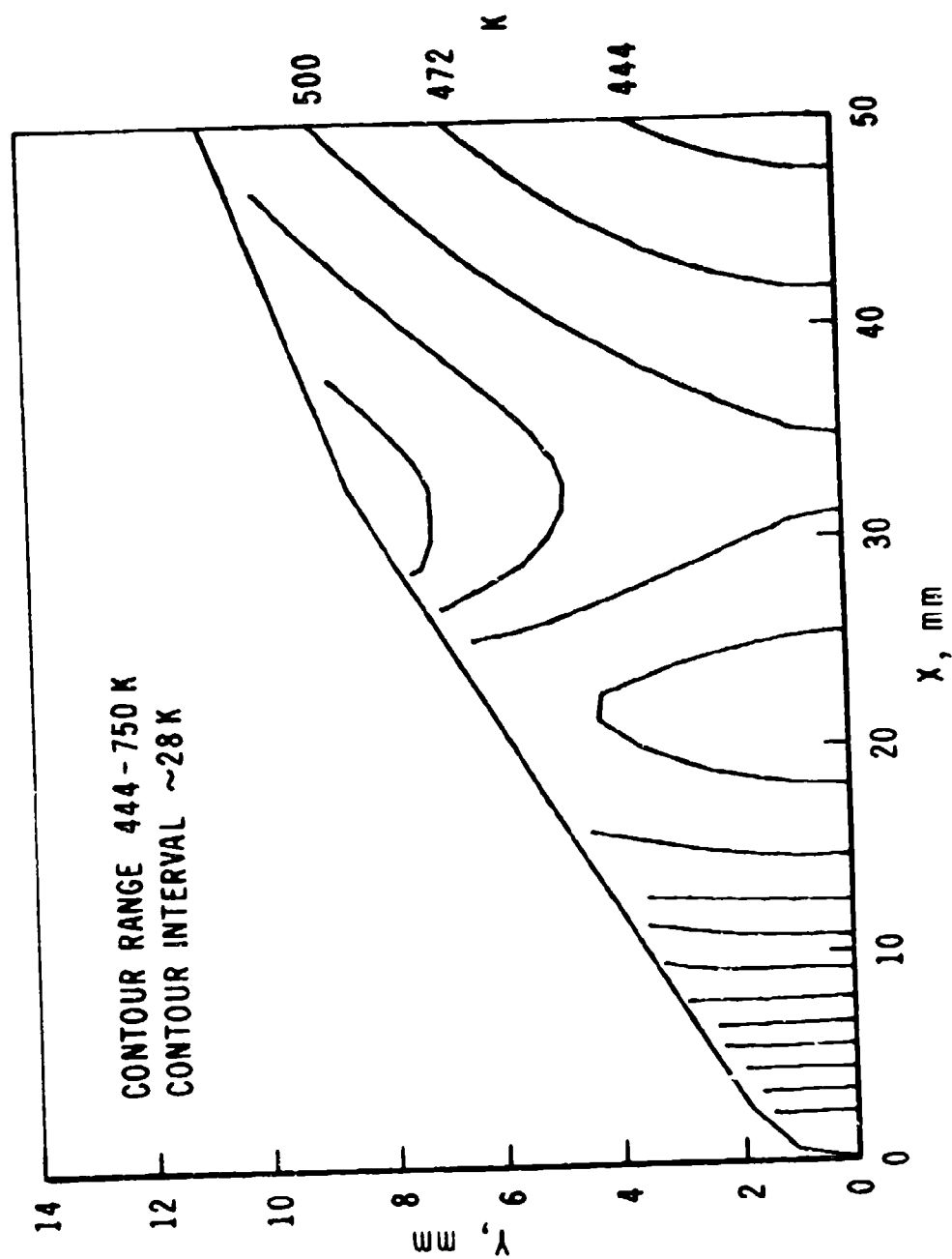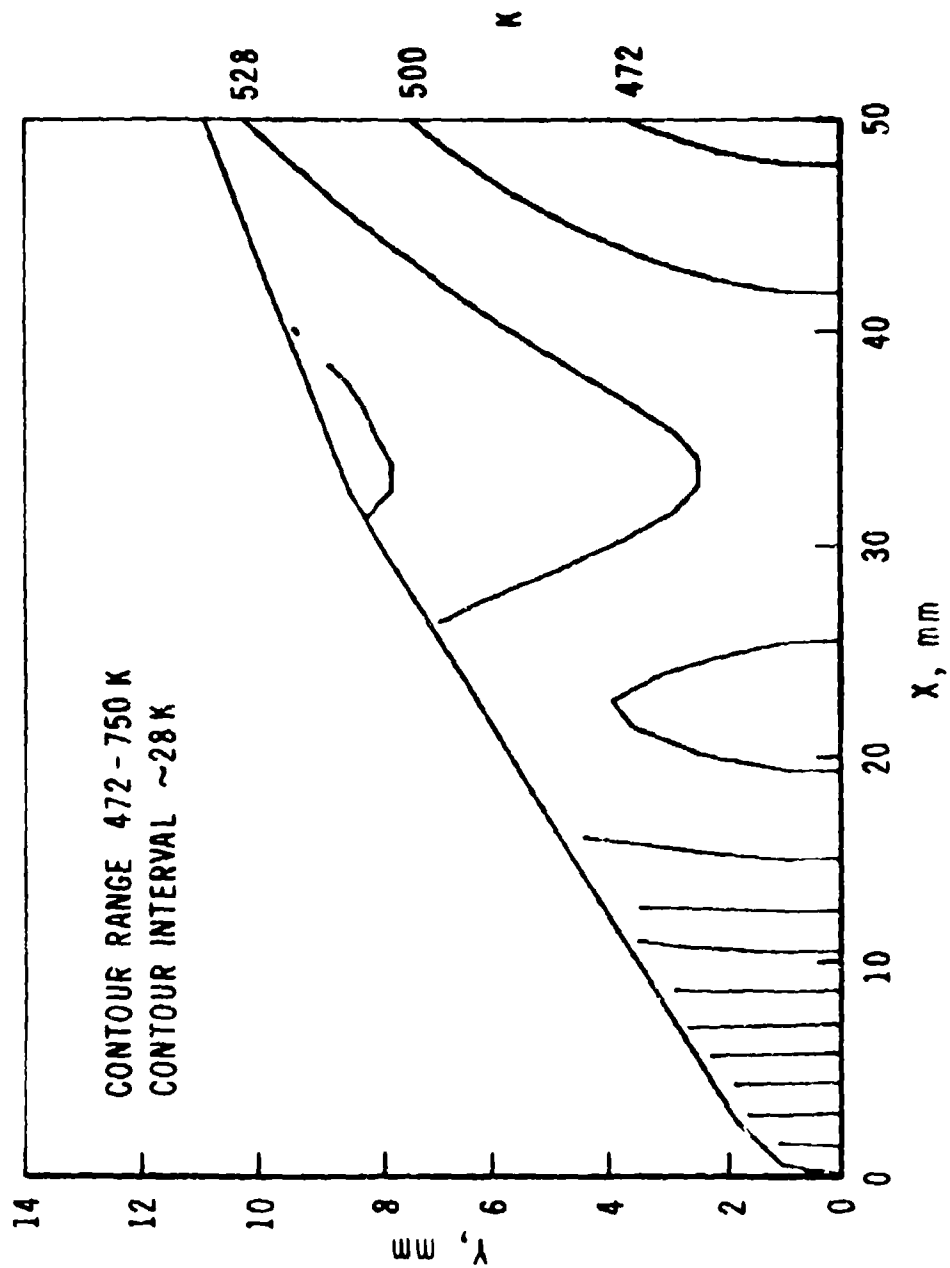CONTOUR INTERVAL ~28 K

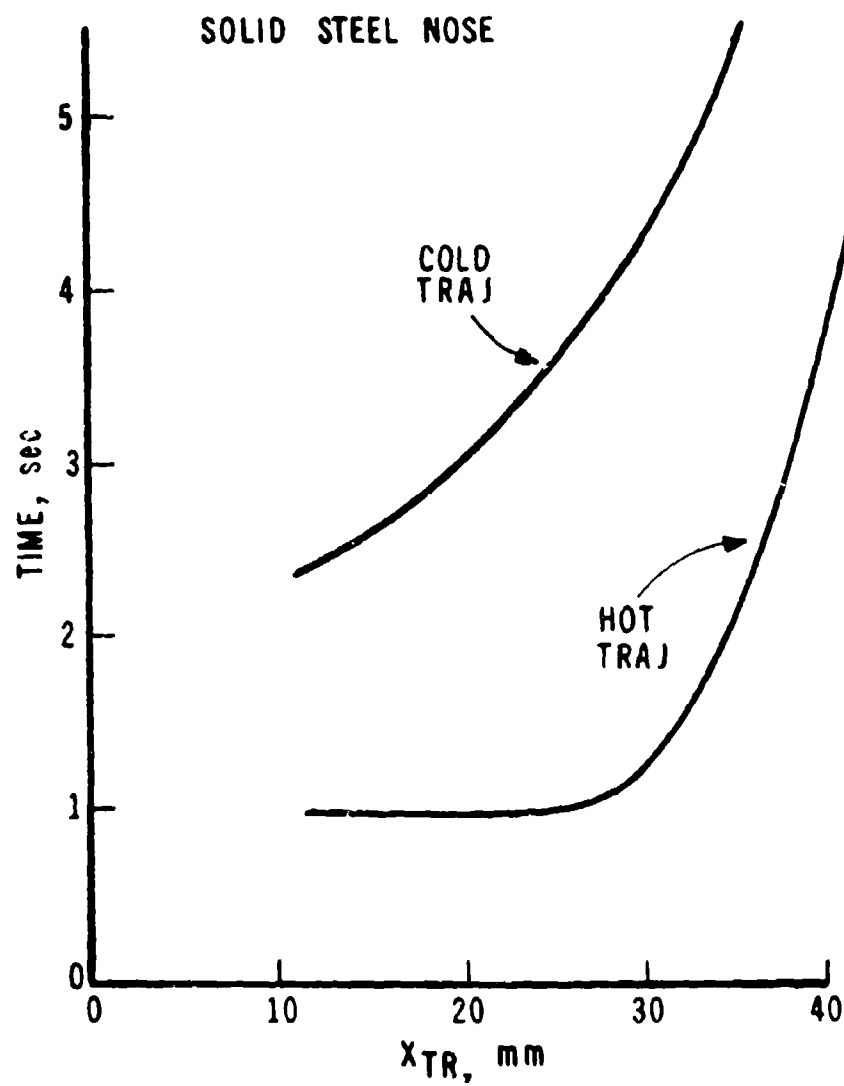Figure 19. Continued

f. Time = 3.0 Seconds

Figure 20. Time for Critical Node to Reach 556K versus Position of Boundary
Layer Transition for High and Low Launch Temperature Conditions

41

REFERENCES

1. Dahn, T.J., Cooper, L., Rafinejad, D., Youngblood, S.B., and Kelly, J.T., "Passive Nosetip Technology (PANT II) Program. Volume I. Inviscid Flow and Heat Transfer Modeling for Reentry Vehicle Nosetips," SAMSO-TR-77-11, Space and Missile Systems Organization, Air Force Systems Command, Los Angeles, California 90009, October 1976.

2. Rafinejad, D., Dahn, T.J., Brink, D.F., Abbett, J.J., and Wolf, C.J., "Passive Nosetip Technology (PANT II) Program. Volume II. Computer Users Manual: ABRES Shape Change Code (ASCC)," SAMSO-TR-77-11, Space and Missile System Organization, Air Force Systems Command, Los Angeles, California 90009, October 1976.

3. Sandhu, S.S., and Murray, A.L., "Reentry Vehicle Technology (REV-TECH) Program. Volume III. Improved Capabilities of the ABRES Shape Change Code (ASCC 79)," Acurex Report TR-79-10/AS, Acurex Corporation/Aerotherm, 485 Clyde Avenue, Mountain View, California 94042, prepared for Space and Missile Systems Organization, Air Force Systems Command, Los Angeles, California 90009, July 1979.

4. Suchsland, K.E., "Aerothermal Assessment of Projectiles Using the ABRES Shape Change Code (ASCC)," Acurex Report TM-80-31-AS, June 1980.

5. Abbett, M.J., Duiven, R.P., Taub, B., and Beck, R.A.S., "Thermal and Structural Analysis of Training Round Nose Caps," Contract Report ARBRL-CR-00455, U.S. Army Ballistic Research Laboratory/ARRADCOM, Aberdeen Proving Ground, Maryland 21005, May 1981 (AD A100712).

6. Crowell, P.G., "Shock Shape Calculation in Body Oriented Coordinates for Specified Surface Pressure," Aerospace Corporation Memo 76-5134.5-019, May 1976.

7. Schwind, Richard G., "Hypersonic Wind Tunnel Tests of Nose Cap Models Utilizing Shape Change for Range Control," Nielsen Engineering and Research, Inc., NEAR TR 184, March 1979.

8. Fleming, G.C., "Maximum Range Test Results of the 105mm, XM797 Training Projectile Conducted Between January and October 1980 at Yuma Proving Ground, Arizona," ASD IR-2-82, December 1981.

9. Loeb, A., LCWSL unpublished experimental data. Private communication.

DISTRIBUTION LIST

No. of
Copies   Organization

No. of
Copies   Organization

12   Administrator
     Defense Technical Info Center
     ATTN: DTIC-DDA
     Cameron Station
     Alexandria, VA 22314

1   Commander
    US Army Materiel Development
       and Readiness Command
    ATTN: DRCDMD-ST
    5001 Eisenhower Avenue
    Alexandria, VA 22333

9   Commander
    US Army Armament Research and
       Development Command
    ATTN: DRDAR-TDC
          DRDAR-TSS
          DRDAR-LCA-F
             Mr. D. Mertz
             Mr. E. Falkowski
             Mr. A. Loeb
             Mr. R. Kline
             Mr. S. Kahn
             Mr. H. Hudgins
    Dover, NJ 07801

1   Commander
    US Army Armament Materiel
       Readiness Command
    ATTN: DRSAR-LEP-L
    Rock Island, IL 61299

1   Director
    US Army Armament Research and
       Development Command
    Benet Weapons Laboratory
    ATTN: DRDAR-LCB-TL
    Watervliet, NY 12189

1   Commander
    US Army Aviation Research and
       Development Command
    ATTN: DRDAV-E
    4300 Goodfellow Blvd.
    St. Louis, MO 63120

1   Director
    US Army Air Mobility Research
       and Development Laboratory
    Ames Research Center
    Moffett Field, CA 94035

1   Commander
    US Army Communications Rsch
       and Development Command
    ATTN: DRSEL-ATDD
    Fort Monmouth, NJ 07703

1   Commander
    US Army Electronics Research
       and Development Command
    Technical Support Activity
    ATTN: DELSD-L
    Fort Monmouth, NJ 07703

2   Commander
    US Army Missile Command
    ATTN: DRSMI-R
          DRSMI-RDK
             Mr. R. Deep
    Redstone Arsenal, AL 35898

1   Commander
    US Army Missile Command
    ATTN: DRSMI-YDL
    Redstone Arsenal, AL 35898

1   Commander
    US Army Tank Automotive
       Command
    ATTN: DRSTA-TSL
    Warren, MI 48090

1   Director
    US Army TRADOC Systems
       Analysis Activity
    ATTN: ATAA-SL
    White Sands Missile Range
       NM 88002

1   Commander
    US Army Research Office
    P. O. Box 12211
    Research Triangle Park
       NC 27709

DISTRIBUTION LIST

No. of Copies	Organization	No. of Copies	Organization

1 Commander
US Naval Air Systems Command
ATTN: AIR-604
Washington, D. C. 20360

2 Commander
David W. Taylor Naval Ship
   Research and Development
   Center
ATTN: Dr. S. de los Santos
      Mr. Stanley Gottlieb
Bethesda, Maryland 20084

4 Commander
US Naval Surface Weapons
   Center
ATTN: Dr. T. Clare, Code DK20
      Mr. P. Daniels
      Mr. D. A. Jones III
      Mr. L. Mason
Dahlgren, VA 22448

4 Commander
US Naval Surface Weapons
   Center
ATTN: Code 312
      Dr. W. Yanta
      Code R44
      Dr. C. Hsieh
      Dr. T. Zien
      Dr. R. U. Jettmar
Silver Spring, MD 20910

1 Commander
US Naval Weapons Center
ATTN: Code 3431, Tech Lib
China Lake, CA 93555

1 Director
NASA Langley Research Center
ATTN: NS-185, Tech Lib
Langley Station
Hampton, VA 23365

2 Commandant
US Army Infantry School
ATTN: ATSH-CD-CSO-OR
Fort Benning, GA 31905

1 ACUREX Corporation/Aerotherm
ATTN: Dr. M. J. Abbett
485 Clyde Avenue
Mountain View, CA 94042

1 AFWL/SUL
Kirtland AFB, NM 87117

1 AVCO Corporation
Research-Advanced Development
   Division
201 Lowell Street
Wilmington, MA 01887

1 Bendix Guided Systems Division
ATTN: MS 2/17A (S. Wasserman)
Teterboro, NJ 97608

1 Nielsen Engineering &
   Research, Inc.
ATTN: Dr. S. Stahara
510 Clyde Avenue
Mountain View, CA 94043

2 Sandia Laboratories
ATTN: Technical Staff,
         Dr. W.L. Oberkampf
      Aeroballistics Division
         5631, H.R. Vaughn
Albuquerque, NM 87115

1 Massachusetts Institute of
   Technology
ATTN: Tech Library
77 Massachusetts Avenue
Cambridge, MA 02139

1 University of Delaware
Mechanical and Aerospace
   Engineering Department
ATTN: Dr. J. E. Danberg
Newark, DE 19711

Aberdeen Proving Ground

Dir, USAMSAA
   ATTN: DRXSY-D
         DRXSY-MP, H. Cohen

44

DISTRIBUTION LIST

Cdr, USATECOM
  ATTN: DRSTE-TO-F

Dir, USACSL, Bldg. E3516, EA
    ATTN: DRDAR-CLB-PA
           DRDAR-CLN
           DRDAR-CLJ-L

USER EVALUATION OF REPORT

Please take a few minutes to answer the questions below; tear out
this sheet, fold as indicated, staple or tape closed, and place
in the mail. Your comments will provide us with information for
improving future reports.

1. BRL Report Number_____

2. Does this report satisfy a need? (Comment on purpose, related
project, or other area of interest for which report will be used.)

_____

_____

_____

3. How, specifically, is the report being used? (Information
source, design data or procedure, management procedure, source of
ideas, etc.)_____

_____

_____

4. Has the information in this report led to any quantitative
savings as far as man-hours/contract dollars saved, operating costs
avoided, efficiencies achieved, etc.? If so, please elaborate.

_____

_____

5. General Comments (Indicate what you think should be changed to
make this report and future reports of this type more responsive
to your needs, more usable, improve readability, etc.)_____

_____

_____

_____

6. If you would like to be contacted by the personnel who prepared
this report to raise specific questions or discuss the topic,
please fill in the following information.

                Name:_____

   Telephone Number:_____

Organization Address:_____

_____

_____